Geosci. Model Dev., 19, 11243–11263, 2026
https://doi.org/10.5194/gmd-19-11243-2026
© Author(s) 2026. This work is distributed under
the Creative Commons Attribution 4.0 License.

Geoscientific Model Development
Open Access
EGU

GEOS-Chem-hyd: enabling source-oriented sensitivity analysis with GEOS-Chem

Samuel O. Akinjole[1], **Jiachen Liu**[1,a], **and Shannon L. Capps**[1]

[1]Department of Civil, Architectural & Environmental Engineering, Drexel University, Philadelphia, 19104, PA, USA
[a]now at: California Air Resources Board, Sacramento, 95814, CA, USA

Correspondence: Shannon L. Capps (shannon.capps@drexel.edu)

Received: 15 September 2025 – Discussion started: 30 October 2025
Revised: 23 September 2026 – Accepted: 20 October 2026 – Published: 25 November 2026

Abstract. Effective environmental policymaking requires accurate quantification of how changes in emissions impact air quality. Chemical transport models, such as GEOS-Chem, are widely used for such analysis. Traditional methods to compute the relative influence of a change in emissions, or the sensitivity of pollutant concentrations to a change in emissions, with these models often suffer from numerical inaccuracies, especially when evaluating nonlinear atmospheric processes. To overcome these limitations, we integrated a novel sensitivity analysis approach leveraging hyperdual numbers into GEOS-Chem, making GEOS-Chem-hyd. The hyperdual step method accurately calculates first- and second-order sensitivities simultaneously and avoids common numerical errors associated with traditional finite difference methods. The real concentrations as well as first- and second-order sensitivities with respect to emissions calculated with GEOS-Chem-hyd align with the values calculated with GEOS-Chem version 14.0.0-rc.3 within expected error. GEOS-Chem-hyd is applied to assess how changes in emissions of nitrogen oxides can alter ozone, particulate matter, ammonium, and biogenic organic aerosol concentrations, demonstrating regional differences and nonlinear influences. As an example of regional variations, the relative influence of increasing nitrogen oxide emissions was to decrease biogenic organic aerosol concentrations in most areas, except in portions of the boreal forests in Siberia. The nonlinear influence of emissions of nitrogen oxides on ozone, ammonium, and biogenic organic aerosol was evidenced by second-order sensitivities on the same order of magnitude as the first-order sensitivities. GEOS-Chem-hyd incurs approximately four times greater computational costs than GEOS-Chem, which is competitive with the three GEOS-Chem model executions required for less accurate second-order sensitivities using the central finite difference method. GEOS-Chem-hyd provides a framework for efficient assessment of the influence of new scientific modules, which are easily incorporated into the sensitivity analysis framework, and supports informed emission control policy development through accurate, source-oriented sensitivity analysis.

1 Introduction

Short-lived air pollution remains one of the most pressing global environmental challenges. Specifically, exposure to ozone (O_3), which forms secondarily from precursor gases such as nitrogen oxides (NO_x), and to particulate matter less than 2.5 µm in aerodynamic diameter ($PM_{2.5}$), which can be directly emitted or formed secondarily in the atmosphere, has been associated with morbidity and premature mortality (Burnett et al., 2014; Turner et al., 2016). Approximately 8.2 % of annual deaths and 4.4 % of disability-adjusted life-years (DALYs) worldwide were attributable to ambient $PM_{2.5}$ exposure with a further 0.8 % of deaths and 0.3 % of DALYs attributable to ambient O_3 in 2023 (Global Burden of Disease Collaborative Network, 2025). Addressing such significant public health concerns requires understanding the nonlinear atmospheric processes that govern pollutant formation and transport. Chemical transport models (CTMs) have proven valuable to scientists and environmental decision-makers for estimating pollutant concentrations. CTMs solve time-dependent, coupled partial differential equations representing the motion and chemical transformations of pollutants based on meteorological inputs and

emissions estimates. Several CTMs have proven useful for understanding nonlinear atmospheric chemistry and its impacts (Anenberg et al., 2019; Keller et al., 2021; Kharol et al., 2013; Le et al., 2020; Li et al., 2021; Pai et al., 2021), improving estimates of emissions (Chen et al., 2021; Henze et al., 2009; Mao et al., 2015; Moon et al., 2024; Qu et al., 2017, 2022; Sitwell et al., 2022; Van Der Graaf et al., 2022; Zhang et al., 2016, 2020; Zhu et al., 2015), and developing efficient emissions control strategies (Capps et al., 2010; Ding et al., 2019; Lyu et al., 2019; Pusede et al., 2016; Tian et al., 2010; Tsimpidi et al., 2007; Turner et al., 2015; Wang et al., 2005; Yang and Zhao, 2023; Zhao et al., 2022). GEOS-Chem is a widely-used, three-dimensional (3D) global CTM representing the multiphase chemistry of the troposphere and stratosphere (Bey et al., 2001; Eastham et al., 2014; Park et al., 2004). Sensitivity analysis in CTMs quantifies how changes in input variables, such as the emissions of select species, affect output variables, such as species concentrations. Several approaches to sensitivity analysis have been developed with select implementations in various CTMs. These approaches are generally classified as three major types: forward, backward, and tagging methods.

Forward sensitivity methods reflect the influence of select model parameters or sources on all modelled results or concentrations. Examples of approaches that provide forward sensitivities are the finite difference method derived from Taylor's theorem, the complex and multicomplex step method (Lantoine et al., 2012; Martins et al., 2003; Squire and Trapp, 1998), dual and hyperdual step methods (Fike and Alonso, 2011), the decoupled direct method (DDM) (Dunker et al., 2002a; Koo et al., 2007), and other tangent linear models (Vukicevic and Errico, 1993). Among these methods, DDM is one of the most prominent and has been more widely applied to CTMs. DDM was introduced to propagate sensitivities through stiff chemical kinetic systems by solving auxiliary sensitivity equations separately from the model equations while retaining the same time steps and numerical approximations (Dunker, 1984). It was subsequently extended to three-dimensional photochemical models (Dunker et al., 2002a; Yang et al., 1997), to particulate matter and aerosol thermodynamics (Koo et al., 2007; Napelenok et al., 2006), and to higher orders, which yield second-order and cross-sensitivities at a per-sensitivity computational cost comparable to that of first-order sensitivity calculations (Cohan et al., 2005; Hakami et al., 2003, 2004; Zhang et al., 2012).

Reverse sensitivity methods reflect the influence on a select receptor of all sources, which is possible through the adjoint method (Errico, 1997). Such instrumented models are usually formulated by appending to the model the inverted call graph of the model with the transpose of the tangent linear model of each line of code inserted (Giering and Kaminski, 1998). This adjoint development approach is known as the discrete approach, which follows the numerical solution of the original model. Since the model development method follows rules understandable by machines, efforts to implement automatic differentiation tools proliferated in the early 2000s (e.g., Alexe and Sandu, 2009; Hascoët and Dauvergne, 2008; Heimbach et al., 2005; Utke et al., 2008). An alternative approach is to derive the analytical derivative and implement the transpose of the analytical derivative, which is known as the continuous method (Giles and Pierce, 2000). Each method provides a first-order sensitivity and is theoretically extensible to higher orders although complications in development or computational costs are entailed in obtaining accurate higher-order sensitivities.

Finally, an alternative approach is tagging parameters. This technique is most straightforward to implement for species whose chemistry is linear or negligible (e.g., Fisher et al., 2017; Ikeda et al., 2017; Kim et al., 2015). For reactive species, tracers may be carried alongside the host chemical mechanism as for O_3 and its precursors in both global and regional models (e.g., Butler et al., 2018; Emmons et al., 2012; Han et al., 2019; Romero-Alvarez et al., 2022; Wang et al., 2011; Whaley et al., 2015) and for aerosol species, including source-oriented treatments that carry the tag through aerosol thermodynamics and microphysics (Kleeman and Cass, 2001; Ying and Kleeman, 2006). Tagging quantifies the absolute contribution of a source to a modelled concentration, whereas the sensitivity methods described above quantify the relative response of that concentration to a change in the source. The two are not interchangeable. For instance, where nonlinear chemistry leads to a precursor inhibiting formation, the sensitivity would be negative while the apportioned contribution remains small and positive (Belis et al., 2021; Cohan et al., 2005; Dunker et al., 2002b; Grewe et al., 2010). Since this approach yields information valuable for source apportionment yet distinct from the derivatives of other sensitivity analysis approaches, implementations of tagging will not be further addressed.

Among the forward sensitivity analysis approaches, the finite difference method has been applied to GEOS-Chem most extensively. Finite difference methods are the most straightforward to implement because no model development is required. First- and second-order sensitivities are calculated based on the Taylor series expansion with two or three model executions, respectively. The finite difference approach has proven valuable for evaluating the impact of a new science module (Sun et al., 2022; Vinken et al., 2011; Yan et al., 2019), conducting mass balance inversions to improve emissions of select species based on satellite observations (Choi et al., 2022; Cooper et al., 2017; Li et al., 2019), and assessing the accuracy of models instrumented to conduct sensitivity analysis (Constantin and Barrett, 2014; Dunker et al., 2002a; Henze et al., 2007; Koo et al., 2007). For the case of analytic inversions of methane (CH_4) emissions, the full Jacobian is constructed from ensembles of hundreds to thousands of perturbation simulations (Maasakkers et al., 2019; Varon et al., 2022). Because CH_4 is simulated as a linear tracer in these inversions, the finite

difference sensitivities are exact apart from round-off error, and higher-order sensitivity methods would offer no benefit. The hyperdual method instead targets nonlinear responses, such as those of O_3 and secondary aerosol, for which finite difference sensitivities depend on the perturbation size.

Prior to this work, the only other instrumented forward sensitivity analysis technique implemented in GEOS-Chem was the complex step method, GEOS-Chem XPLEX (Constantin and Barrett, 2014). The complex step method is derived from the Taylor series expansion as is the finite difference method, but this approach differs because the perturbation is propagated in imaginary space. Since no subtraction occurs in the real space, the cancellation error is eliminated. Although truncation errors still exist because the third and higher-order terms are ignored from the Taylor series expansion, they can be minimized by choosing a very small step size (e.g., $O(10^{-20})$). This method was applied to the adjoint of GEOS-Chem, which allows for the calculation of a unique type of second-order sensitivity.

Two operator overloading approaches similar to the complex step method enable the direct computation of first-order, second-order, and cross sensitivities. The multicomplex step method developed by Lantoine et al. (2012) and the hyperdual step method developed by Fike and Alonso (2011) arise from the Taylor series expansion yet in distinct number spaces such that the outcome is not subject to subtractive cancellation or truncation errors due to the unique properties of multicomplex or hyperdual numbers. The resulting higher-order derivatives improve the accuracy of the Taylor expansion and allow nonlinear influences of parameters to be quantified (Liu and Capps, 2026). Neither had previously been implemented in GEOS-Chem.

The adjoint method efficiently provides receptor-oriented sensitivities of a concentration-based cost function. Henze et al. (2007) developed the GEOS-Chem adjoint model as have others for select CTMs (e.g., CMAQ-adj; Zhao et al., 2020) or subsets of them (e.g., WRF-CO_2; Zheng et al., 2018). The GEOS-Chem adjoint has proven tremendously valuable for atmospheric scientists and environmental decision-makers. The cost functions for which sensitivities are calculated may be location-specific, such as a combined statistical area to be regulated (e.g., Lyu et al., 2021; Turner et al., 2015); exposure metric-specific, such as ozone effects on plants (e.g., Lapina et al., 2014); or a combination of functions of different species or metrics (e.g., Lyu et al., 2019). Furthermore, scientists have leveraged this form of augmented model to design or conduct inverse modelling of emissions estimates using observations of air pollutants, especially from satellites (Chen et al., 2021; Choi et al., 2022; Cooper et al., 2017; Elbern et al., 2010; Li et al., 2019; Moon et al., 2024; Qu et al., 2017).

This paper describes the implementation, evaluation, and demonstration of the hyperdual step method in GEOS-Chem. The hyperdual method is complementary to the receptor-oriented sensitivities calculated with the GEOS-Chem adjoint (Henze et al., 2007): the hyperdual method resolves the influence of a specific set of sources on the entire set of concentrations (Jacobian rows), while the adjoint resolves the influence of all sources on a select set of concentrations (Jacobian columns). The hyperdual approach additionally yields higher-order sensitivities with respect to the same source in a single model run. Although adjoint-on-adjoint code could be implemented to calculate second-order sensitivities, applications of the GEOS-Chem adjoint often assess the first-order sensitivities to be adequate for the extent of change assessed in the system or involve iteration in which the sensitivities are recalculated at different emissions levels. Liu et al. (2024) developed a Fortran library for overloading operators with hyperdual numbers, HDMod (https://github.com/atmmod/HDMod, last access: 16 November 2026) by translating and substantially augmenting the C++-based library of Fike and Alonso (2011). This operator overloading approach was applied in the Community Multiscale Air Quality Model (CMAQ) as the first application of hyperdual numbers in an atmospheric CTM (Liu et al., 2024).

Here, the GEOS-Chem model is augmented with the hyperdual step method to create GEOS-Chem-hyd. In Sect. 2, we describe hyperdual numbers, their implementation in GEOS-Chem, and the method for evaluating GEOS-Chem-hyd. In Sect. 3.1–3.2, we evaluate the accuracy and computational cost of GEOS-Chem-hyd. In Sect. 3.3, we demonstrate the usefulness of GEOS-Chem-hyd by evaluating the response of O_3, $PM_{2.5}$, ammonium (NH_4^+), and biogenic organic aerosol (OA_{bio}) concentrations to perturbations in domain-wide NO_x emissions over a four-week simulation. To the best of our knowledge, this is the first augmentation of GEOS-Chem that accurately computes both first- and second-order sensitivities of concentrations with respect to select emissions.

2 Methods

2.1 Hyperdual numbers

Fike and Alonso (2011) introduced hyperdual numbers to compute numerically exact first- and second-order derivatives simultaneously. A hyperdual number, H, is defined as:

$$H = a_0 + a_1\epsilon_1 + a_2\epsilon_2 + a_{12}\epsilon_{12} \quad (1)$$

where, a_0, a_1, a_2, and a_{12} are real number coefficients, and ϵ_1, ϵ_2, and ϵ_{12} are non-real components analogous to the imaginary component, i, of a complex number. These non-real components follow these rules:

$$\epsilon_1^2 = \epsilon_2^2 = \epsilon_{12}^2 = 0 \quad (2)$$

$$\epsilon_1 \neq \epsilon_2 \neq \epsilon_{12} \neq 0 \quad (3)$$

$$\epsilon_1\epsilon_2 = \epsilon_2\epsilon_1 = \epsilon_{12} \quad (4)$$

The square of each non-real component equals zero (Eq. 2). However, these components themselves are not equal to zero

(Eq. 3). Multiplication of non-real components is commutative (Eq. 4), while multiplying ϵ_1 and ϵ_2 equals the third non-real component ϵ_{12} (Eq. 4). Here, ϵ_{12} denotes a nonzero hyperdual basis element; however, its coefficient in a given variable may be zero at initialization and become nonzero only after nonlinear propagation. Hyperdual arithmetic leverages these properties to precisely calculate derivatives using Taylor series expansions (Fike and Alonso, 2011; Liu et al., 2024). Perturbations are either additive or multiplicative, as with finite difference methods. In this work, we use multiplicative perturbations (5 % unless stated otherwise) because they provide a physically meaningful representation of emission scaling. Policy-relevant emission adjustments are typically expressed as fractional changes (e.g., percentage reductions), which correspond naturally to multiplicative perturbations and provide consistent scaling across grid cells with widely varying emission magnitudes. To perturb a scalar function, $f(x)$, multiplicatively, we multiply x by a hyperdual number, $H_a = 1+a_1\epsilon_1+a_2\epsilon_2+0\epsilon_{12}$. Expanding $f(xH_a)$ yields a Taylor series:

$$\begin{aligned} f(xH_a) = {} & f(x) + (xa_1\epsilon_1 + xa_2\epsilon_2) f'(x) \\ & + \frac{1}{2!}(xa_1\epsilon_1 + xa_2\epsilon_2)^2 f''(x) \\ & + \frac{1}{3!}(xa_1\epsilon_1 + xa_2\epsilon_2)^3 f'''(x) + \dots \end{aligned} \tag{5}$$

Applying hyperdual properties (Eqs. 2–4) simplifies Eq. (5) to

$$\begin{aligned} f(xH_a) = {} & f(x) + (xa_1\epsilon_1 + xa_2\epsilon_2) f'(x) \\ & + x^2 a_1 a_2 \epsilon_{12} f''(x) \end{aligned} \tag{6}$$

where $f(xH_a)$ is a hyperdual number, and the other terms in Eq. (5) are zero due to the properties of hyperdual numbers. Rearranging and extracting the non-real components of the left-hand side and right-hand side of Eq. (6), provides numerically exact derivatives:

$$f'(x) = \frac{\epsilon_1 \,\mathrm{part}\left[f(xH_a)\right]}{xa_1} = \frac{\epsilon_2 \,\mathrm{part}\left[f(xH_a)\right]}{xa_2} \tag{7}$$

$$f''(x) = \frac{\epsilon_{12} \,\mathrm{part}\left[f(xH_a)\right]}{x^2 a_1 a_2} \tag{8}$$

where the notation ϵ_1 part[], ϵ_2 part[], and ϵ_{12} part[] represents the extraction of coefficients associated with ϵ_1, ϵ_2, and ϵ_{12}, respectively. The extracted coefficients are the a_1, a_2, and a_{12} components of the function evaluation. Unlike the finite difference method, these expressions do not involve numerical subtraction or truncation of higher-order terms. Therefore, hyperdual arithmetic eliminates common numerical issues like subtractive cancellation and truncation errors. This method is extensible to vector-valued functions, $f(\boldsymbol{x})$, where $\boldsymbol{x} = [x_1, x_2, \dots, x_n]$. Perturbing a single variable, x_1, yields first and second derivatives with respect to x_1 as shown:

$$\frac{\partial f(\boldsymbol{x})}{\partial x_1} = \frac{\epsilon_1 \,\mathrm{part}\left[f\left(\boldsymbol{x}H_{a,x_1}\right)\right]}{x_1 a_1} = \frac{\epsilon_2 \,\mathrm{part}\left[f\left(\boldsymbol{x}H_{a,x_1}\right)\right]}{x_1 a_2} \tag{9}$$

$$\frac{\partial^2 f(\boldsymbol{x})}{\partial x_1^2} = \frac{\epsilon_{12} \,\mathrm{part}\left[f\left(\boldsymbol{x}H_{a,x_1}\right)\right]}{{x_1}^2 a_1 a_2} \tag{10}$$

Additionally, hyperdual arithmetic allows for simultaneous perturbation of multiple variables, facilitating efficient cross-sensitivity computation. Perturbing two independent variables, x_1 and x_2, yields the following derivatives:

$$\frac{\partial f(\boldsymbol{x})}{\partial x_1} = \frac{\epsilon_1 \,\mathrm{part}\left[f(\boldsymbol{x}H_a)\right]}{x_1 a_1} \tag{11}$$

$$\frac{\partial f(\boldsymbol{x})}{\partial x_2} = \frac{\epsilon_2 \,\mathrm{part}\left[f(\boldsymbol{x}H_a)\right]}{x_2 a_2} \tag{12}$$

$$\frac{\partial^2 f(\boldsymbol{x})}{\partial x_1 \partial x_2} = \frac{\epsilon_{12} \,\mathrm{part}\left[f(\boldsymbol{x}H_a)\right]}{x_1 x_2 a_1 a_2} \tag{13}$$

where the first-order sensitivities of each independent variable are given by Eqs. (11)–(12) and the cross-sensitivity in Eq. (13). This versatility makes the hyperdual step method particularly suitable for evaluating sensitivities in computationally demanding and highly nonlinear systems, such as CTMs.

2.2 Implementation of the hyperdual step method in GEOS-Chem

GEOS-Chem simulates concentrations by solving the generalized continuity equation for an Eulerian 3-D grid (Seinfeld and Pandis, 2016):

$$\begin{aligned} \frac{\partial C_i}{\partial t} = {} & -\nabla\cdot(\boldsymbol{u}C_i) + \nabla\cdot(\mathbf{K}\nabla C_i) \\ & + R_i(C_1, C_2, \dots, C_n) + E_i - S_i \end{aligned} \tag{14}$$

where C_i is the concentration of species i, $\boldsymbol{u}$ is the wind velocity vector, $\mathbf{K}$ is the turbulent diffusivity, R_i is the chemical production rate for species i, E_i is the emission rate for species i, and S_i is the removal flux for species i. Here, the hyperdual step method is implemented in GEOS-Chem version 14.0.0-rc.3. The model is executed at $4^\circ \times 5^\circ$ spatial resolution with 72 vertical layers. MERRA-2 meteorological fields (Gelaro et al., 2017) and global anthropogenic emissions from the CEDS v2 inventory (O'Rourke et al., 2021) are used as inputs, with the configuration settings available at https://doi.org/10.5281/zenodo.22699829 (Akinjole et al., 2026b). Here, we use the full chemistry gas-phase mechanism, which employs a Rosenbrock solver generated by the Kinetic PreProcessor (KPP) (Sandu and Sander, 2006). We select the aerosol option that employs the forward mode of ISORROPIA for aerosol thermodynamics (Fountoukis and Nenes, 2007; Pye et al., 2009). Dry deposition utilizes a standard resistance-in-series scheme (Wesely, 1989) with several modifications (Jaeglé et al., 2018;

Wang et al., 1998), and wet deposition follows a scheme that includes washout and rainout of soluble species (Liu et al., 2001). Transport follows the TPCORE advection scheme (Lin and Rood, 1996), while the non-local PBL mixing scheme is used (Lin and McElroy, 2010). For all the simulations described here, the timesteps were 20 min for chemistry and 10 min for transport (Philip et al., 2016).

The hyperdual version of GEOS-Chem, GEOS-Chem-hyd, enables the calculation of derivatives using the hyperdual step method. The appropriate variables are converted to hyperdual numbers, which requires an operator overloading library (Fike and Alonso, 2011). For GEOS-Chem-hyd, we employ the HDMod Fortran library developed by Liu et al. (2024), which was further enhanced to support additional array operations specific to the GEOS-Chem source code. The computational cost for a hyperdual calculation ranges from 4 to 14 times that of a real number calculation (Fike and Alonso, 2011). Although all real variables in GEOS-Chem could have been converted to hyperdual type, we reduced the computational cost by selectively converting the necessary variables. Specifically, the species concentration array and all other active variables that propagate sensitivities to the species concentration array across GEOS-Chem were changed to the hyperdual type (Fig. 1). Here, active variables are defined as those that are impacted by emissions or initial concentrations. The corresponding derivatives are inherently evaluated through every overloaded operation as the first-order derivative information is held in the ϵ_1 and ϵ_2 components while the second-order derivative information is contained in the ϵ_{12} component. Additional diagnostics were added to obtain the non-real components for species concentrations and aerosol mass using the same structure as those of the real components. Likewise, the restart capability was extended for the non-real components to enable sensitivity propagations for longer simulations.

GEOS-Chem has several modules that are sufficiently complicated to require independent, iterative development and evaluation. The chemistry and aerosol modules were unit-tested. In gas phase chemistry, the gas-phase rate constants in the kinetic preprocessor were maintained as real rather than hyperdual to ensure numerical stability and increase computational efficiency without meaningfully reducing the agreement of the hyperdual sensitivities with finite difference or hybrid sensitivities. The Harmonized Emissions Component (HEMCO) is a standalone model for emissions (Lin et al., 2021). For the purposes of introducing GEOS-Chem-hyd, the emission routines that interface with GEOS-Chem Classic (GCClassic) are made compatible with hyperdual operations. The full HEMCO-hyd is work currently in progress. The first-order sensitivities from the GEOS-Chem external arrays to the HEMCO arrays evaluate well against finite difference (Fig. S1 in the Supplement), and the second-order sensitivities evaluate well against the hybrid method (Fig. S2). The current implementation is limited to GCClassic; support for GEOS-Chem High Performance (GCHP) and

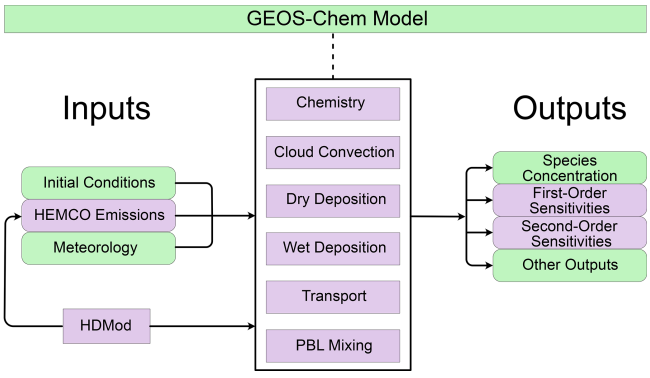

Figure 1. A schematic of the GEOS-Chem-hyd model. Purple components highlight modifications to the standard model for hyperdual calculations, utilizing the overloading library, HDMod. First- and second-order sensitivities are calculable from new outputs of hyperdual calculations. Note that only necessary elements of HEMCO have yet been hyperdualized for the testing of GEOS-Chem-hyd and the remaining components are forthcoming.

for specialized configurations such as the TOMAS aerosol microphysics scheme constitutes future work.

Finally, the refinements to the inorganic aerosol thermodynamics module, ISORROPIA, were the most extensive. Accordingly, we extended a standalone version of ISORROPIA developed for testing conditions encountered in GEOS-Chem (Berman et al., 2023) to develop ISORROPIA-hyd with stable sensitivities over the extensive range of conditions encountered throughout the troposphere. We made three types of refinement in the hyperdual space. First, the nested nature of ISORROPIA leads to activity coefficients being calculated at nearly every set of aqueous concentrations on the path to determining the equilibrium solution. Accordingly, we kept only the real part of these calculations, which influence the concentrations along the solution path. This adjustment was shown not to alter the first- or second-order sensitivities substantially in the usual case of a stable result while eliminating the rare cases in which activity coefficient calculations led to extremely large sensitivities. This approach also improved computational efficiency marginally. Secondly, we refined the quadratic solution in the two limiting cases of the elements of the discriminant, $\sqrt{b^2-4ac}$. In the first, $b^2 \gg |4ac|$, so that $-b+\sqrt{b^2-4ac}$ subtracts nearly equal floating-point numbers. In this case, the root loses precision, so we instead adopted the numerically stable quadratic formulation recommended by Press et al. (2007), which was implemented in HETP (Miller et al., 2024). In the second, $b^2 \to 4ac$, so that the discriminant approaches zero. In this case, the root itself remains smooth as the two roots merge, but its first and second derivatives scale as $D^{-1/2}$ and $D^{-3/2}$ and diverge. For this case, we introduced safeguards that detect the near-degenerate configuration and prevent the amplified derivatives from propagating while maintaining the real result. Finally, the equilibrium sub-cases for

the sulphate-poor and sodium-poor (G5) and the sulphate-poor and sodium-rich (H6) are solved by bisection, which is non-differentiable. We, therefore, augment bisection with a two-step post-convergence Newton–Raphson refinement following previous works (Capps et al., 2012; Griewank and Walther, 2008). The analytic residual derivatives, which were generated with Tapenade (Hascoet and Pascual, 2013), make this step differentiable. Table S1 in the Supplement summarizes the modifications implemented in ISORROPIA to ensure a stable hyperdual formulation.

2.3 Evaluating sensitivities from GEOS-Chem-hyd

The implementation of a novel sensitivity analysis technique in a model requires evaluation to ensure that the behaviour of the underlying model is represented accurately by the augmented model (Hakami et al., 2004; Napelenok et al., 2006; Zhang et al., 2012). First, we evaluated the real components to ensure that the modelled concentrations of the augmented model are consistent with the base model. Then, we designed evaluations of first- and second-order sensitivities calculated by the hyperdual step method for a representative set of relationships of concentrations to emissions. Semi-normalization allows the sensitivities to be expressed in the same units as the numerator in response to a fractional change in the denominator, which is particularly useful when estimating relative concentration responses to fractional emissions changes using a Taylor-series approximation. We apply multiplicative perturbations of magnitude unity in the dual space in GEOS-Chem-hyd to produce semi-normalized sensitivities without the need for post-processing.

We illustrate the nomenclature with the first-order semi-normalized sensitivity of O_3 concentrations at the ground layer, $C_{O_3,i,j,l=0,t}$, for a time-averaged simulation to a persistent, domain-wide NO_x emission. Although any subset of species, space, and time could be selected for investigation, these perturbations are applied uniformly to every grid cell and every emission timestep, so the emissions in the denominator are represented by the domain-wide, episode-total emissions:

$$E_{\mathrm{NO}_x,\mathrm{dom}} = \sum_{i,j,l}\sum_{t=0}^{t_\mathrm{f}} E_{\mathrm{NO}_x,i,j,l,t} \tag{15}$$

where subscripts i, j, and l are the longitudinal, latitudinal, and vertical indices for the grid cell; t is the timestep from the start of the model simulation; and t_f is the final timestep of the model simulation. Here, we perturb emissions at every 20 min chemistry timestep throughout a 24 h episode. Accordingly, the application of this perturbation using the central finite difference method is given by

$$\left.\overline{\frac{\partial C_{O_3,i,j,l=0,t}}{\partial E^{\mathrm{def}}_{\mathrm{NO}_x,\mathrm{dom}}}}\right|_t E^{\mathrm{def}}_{\mathrm{NO}_x,\mathrm{dom}} \approx \frac{\left.\overline{C^{\mathrm{inc}}_{O_3,i,j,l=0,t}}\right|_t - \left.\overline{C^{\mathrm{dec}}_{O_3,i,j,l=0,t}}\right|_t}{E^{\mathrm{inc}}_{\mathrm{NO}_x,\mathrm{dom}} - E^{\mathrm{dec}}_{\mathrm{NO}_x,\mathrm{dom}}} E^{\mathrm{def}}_{\mathrm{NO}_x,\mathrm{dom}} \tag{16}$$

the superscript inc indicates a positive perturbation in real space; the superscript dec indicates a negative perturbation in real space; and the superscript def indicates that no real perturbation was applied. Another advantage of semi-normalized sensitivities is that the sum of the emissions over the episode is not required to calculate semi-normalized sensitivities in the finite difference method as

$$\left.\overline{\frac{\partial C_{O_3,i,j,l=0,t}}{\partial E^{\mathrm{def}}_{\mathrm{NO}_x,\mathrm{dom}}}}\right|_t E^{\mathrm{def}}_{\mathrm{NO}_x,\mathrm{dom}} \approx \frac{\left.\overline{C^{\mathrm{inc}}_{O_3,i,j,l=0,t}}\right|_t - \left.\overline{C^{\mathrm{dec}}_{O_3,i,j,l=0,t}}\right|_t}{2p} \tag{17}$$

where p is the magnitude of the multiplicative perturbation. Unless stated otherwise, the perturbation sizes used in this manuscript are $\pm 5\,\%$ for the finite difference domain-wide emissions ($p = 0.05$). We found this perturbation size to be large enough to observe beyond numerical noise while still small enough to represent local emission changes for most species. These semi-normalized sensitivities have the unit of parts per billion (ppb) with respect to a fractional change in the emissions for the species concentration collection and micrograms per meter cubed ($\mu g\,m^{-3}$) with respect to a fractional change in the emissions for the aerosol mass collection.

The first-order semi-normalized sensitivity of time-averaged, ground-level O_3 concentrations to domain-wide NO_x emissions is calculated with a multiplicative hyperdual perturbation, $H_a = 1.0 + a_1\epsilon_1 + a_2\epsilon_2$, using the hyperdual step method as

$$\begin{aligned}\left.\overline{\frac{\partial C_{O_3,i,j,l=0,t}}{\partial E^{\mathrm{def}}_{\mathrm{NO}_x,\mathrm{dom}}}}\right|_t E^{\mathrm{def}}_{\mathrm{NO}_x,\mathrm{dom}} &= \frac{\epsilon_1\,\mathrm{part}\left[\left.\overline{C^{\mathrm{def}}_{O_3,i,j,l,t}}\right|_t\right]}{a_1 E^{\mathrm{def}}_{\mathrm{NO}_x,\mathrm{dom}}} E^{\mathrm{def}}_{\mathrm{NO}_x,\mathrm{dom}} \\ &= \frac{\epsilon_2\,\mathrm{part}\left[\left.\overline{C^{\mathrm{def}}_{O_3,i,j,l,t}}\right|_t\right]}{a_2 E^{\mathrm{def}}_{\mathrm{NO}_x,\mathrm{dom}}} E^{\mathrm{def}}_{\mathrm{NO}_x,\mathrm{dom}}\end{aligned} \tag{18}$$

where the persistent perturbation in ϵ_1 space is a_1 and ϵ_2 space is a_2. This expression can be further simplified to

$$\begin{aligned}\overline{\frac{\partial C_{\mathrm{O}_3,i,j,l=0,t}}{\partial E^{\mathrm{def}}_{\mathrm{NO}_x,\mathrm{dom}}}}\Bigg|_t E^{\mathrm{def}}_{\mathrm{NO}_x,\mathrm{dom}} &= \frac{\epsilon_1\,\mathrm{part}\left[\overline{C^{\mathrm{def}}_{\mathrm{O}_3,i,j,l,t}}\Big|_t\right]}{a_1} \\ &= \frac{\epsilon_2\,\mathrm{part}\left[\overline{C^{\mathrm{def}}_{\mathrm{O}_3,i,j,l,t}}\Big|_t\right]}{a_2} \end{aligned} \tag{19}$$

where the first-order semi-normalized sensitivity can be obtained from either the ϵ_1 or the ϵ_2 part divided by the respective perturbation in ϵ_1 space (a_1) or ϵ_2 space (a_2).

For the second-order sensitivities, the central finite difference method is second-order accurate. However, if the relationship is nonlinear, the result is highly dependent on perturbation sizes because the altered model states affect the response (Zhang et al., 2012). As such, a hybrid hyperdual-central finite difference (hybrid) method is used, which reduces the dependence on the model state changing (Liu et al., 2024). The second-order semi-normalized sensitivity of the average concentration with respect to a persistent perturbation in emissions using the hybrid method can be expressed as:

$$\begin{aligned}&\overline{\frac{\partial^2 C_{\mathrm{O}_3,i,j,l=0,t}}{\partial {E^{\mathrm{def}}_{\mathrm{NO}_x,\mathrm{dom}}}^2}}\Bigg|_t \left(E^{\mathrm{def}}_{\mathrm{NO}_x,\mathrm{dom}}\right)^2 \\ &\approx \frac{\frac{\epsilon_2\,\mathrm{part}\left[\overline{C^{\mathrm{inc}}_{\mathrm{O}_3,i,j,l,t}}\Big|_t\right]}{a_2 E^{\mathrm{inc}}_{\mathrm{NO}_x,\mathrm{dom}}} - \frac{\epsilon_2\,\mathrm{part}\left[\overline{C^{\mathrm{dec}}_{\mathrm{O}_3,i,j,l,t}}\Big|_t\right]}{b_2 E^{\mathrm{dec}}_{\mathrm{NO}_x,\mathrm{dom}}}}{E^{\mathrm{inc}}_{\mathrm{NO}_x,\mathrm{dom}} - E^{\mathrm{dec}}_{\mathrm{NO}_x,\mathrm{dom}}}\left(E^{\mathrm{def}}_{\mathrm{NO}_x,\mathrm{dom}}\right)^2 \end{aligned} \tag{20}$$

where the inc case is perturbed in the real space by 5 % and dual spaces by $H_a = 1.0 + a_1\epsilon_1 + a_2\epsilon_2$ and the dec case is perturbed in the real space by -5 % and dual spaces by $H_b = 1.0 + b_1\epsilon_1 + b_2\epsilon_2$. Depending on the choice of the hyperdual perturbation, the numerator is evaluated from either the ϵ_1 or the ϵ_2 part. The lowest denominator is the perturbation size in the real part, which simplifies as

$$\begin{aligned}&\overline{\frac{\partial^2 C_{\mathrm{O}_3,i,j,l=0,t}}{\partial {E^{\mathrm{def}}_{\mathrm{NO}_x,\mathrm{dom}}}^2}}\Bigg|_t \left(E^{\mathrm{def}}_{\mathrm{NO}_x,\mathrm{dom}}\right)^2 \\ &\approx \frac{\epsilon_2\,\mathrm{part}\left[\overline{C^{\mathrm{inc}}_{\mathrm{O}_3,i,j,l,t}}\Big|_t\right]}{2a_2\,p\,(1+p)} - \frac{\epsilon_2\,\mathrm{part}\left[\overline{C^{\mathrm{dec}}_{\mathrm{O}_3,i,j,l,t}}\Big|_t\right]}{2b_2\,p\,(1-p)} \end{aligned} \tag{21}$$

The simplified hyperdual step method semi-normalized second-order sensitivities can be expressed as

$$\overline{\frac{\partial^2 C_{\mathrm{O}_3,i,j,l=0,t}}{\partial {E^{\mathrm{def}}_{\mathrm{NO}_x,\mathrm{dom}}}^2}}\Bigg|_t \left(E^{\mathrm{def}}_{\mathrm{NO}_x,\mathrm{dom}}\right)^2 = \frac{\epsilon_{12}\,\mathrm{part}\left[\overline{C^{\mathrm{def}}_{\mathrm{O}_3,i,j,l,t}}\Big|_t\right]}{a_1 a_2} \tag{22}$$

In this case, only one simulation is run with a hyperdual perturbation of $H_a = 1.0 + a_1\epsilon_1 + a_2\epsilon_2$, where the emissions in the denominator also cancel out, and the second-order semi-normalized sensitivity is obtained from the ϵ_{12} part divided by the product of the perturbations, $a_1 a_2$.

In addition, cross-sensitivities can be obtained using hybrid and the hyperdual step methods. To illustrate, the semi-normalized cross-sensitivity of ground-level O_3 concentrations at a given time, $C_{\mathrm{O}_3,i,j,l=0,t}$, to NO_x and ISOP emissions using the hybrid method is given by

$$\begin{aligned}&\overline{\frac{\partial^2 C_{\mathrm{O}_3,i,j,l=0,t}}{\partial E^{\mathrm{def}}_{\mathrm{NO}_x,\mathrm{dom}}\partial E^{\mathrm{def}}_{\mathrm{ISOP},\mathrm{dom}}}}\Bigg|_t \left(E^{\mathrm{def}}_{\mathrm{NO}_x,\mathrm{dom}} E^{\mathrm{def}}_{\mathrm{ISOP},\mathrm{dom}}\right) \\ &\approx \frac{\frac{\epsilon_2\,\mathrm{part}\left[\overline{C^{\mathrm{inc}}_{\mathrm{O}_3,i,j,l,t}}\Big|_t\right]}{a_2 E^{\mathrm{def}}_{\mathrm{ISOP},\mathrm{dom}}} - \frac{\epsilon_2\,\mathrm{part}\left[\overline{C^{\mathrm{dec}}_{\mathrm{O}_3,i,j,l,t}}\Big|_t\right]}{b_2 E^{\mathrm{def}}_{\mathrm{ISOP},\mathrm{dom}}}}{E^{\mathrm{inc}}_{\mathrm{NO}_x,\mathrm{dom}} - E^{\mathrm{dec}}_{\mathrm{NO}_x,\mathrm{dom}}} \\ &\cdot \left(E^{\mathrm{def}}_{\mathrm{NO}_x,\mathrm{dom}} E^{\mathrm{def}}_{\mathrm{ISOP},\mathrm{dom}}\right) \end{aligned} \tag{23}$$

where the real perturbations are applied to the NO_x emissions, $E_{\mathrm{NO}_x,i,j,l,t}$, and the hyperdual perturbations are applied to the ϵ_2 space of the ISOP emission, $E_{\mathrm{ISOP},i,j,l,t}$. Practically, this expression simplifies to

$$\begin{aligned}&\overline{\frac{\partial^2 C_{\mathrm{O}_3,i,j,l=0,t}}{\partial E^{\mathrm{def}}_{\mathrm{NO}_x,\mathrm{dom}}\partial E^{\mathrm{def}}_{\mathrm{ISOP},\mathrm{dom}}}}\Bigg|_t \left(E^{\mathrm{def}}_{\mathrm{NO}_x,\mathrm{dom}} E^{\mathrm{def}}_{\mathrm{ISOP},\mathrm{dom}}\right) \\ &\approx \frac{\epsilon_2\,\mathrm{part}\left[\overline{C^{\mathrm{inc}}_{\mathrm{O}_3,i,j,l,t}}\Big|_t\right]}{2a_2\,p} - \frac{\epsilon_2\,\mathrm{part}\left[\overline{C^{\mathrm{dec}}_{\mathrm{O}_3,i,j,l,t}}\Big|_t\right]}{2b_2\,p} \end{aligned} \tag{24}$$

The simplified semi-normalized cross-sensitivity using the hyperdual step method requires only one simulation with a hyperdual perturbation of NO_x emission in the ϵ_1 space, $H_a = 1 + a_1\epsilon_1$ and ISOP emission in the ϵ_2 space, $H_b = 1 + b_2\epsilon_2$, and is given by

$$\begin{aligned}&\overline{\frac{\partial^2 C_{\mathrm{O}_3,i,j,l=0,t}}{\partial E^{\mathrm{def}}_{\mathrm{NO}_x,\mathrm{dom}}\partial E^{\mathrm{def}}_{\mathrm{ISOP},\mathrm{dom}}}}\Bigg|_t \left(E^{\mathrm{def}}_{\mathrm{NO}_x,\mathrm{dom}} E^{\mathrm{def}}_{\mathrm{ISOP},\mathrm{dom}}\right) \\ &= \frac{\epsilon_{12}\,\mathrm{part}\left[\overline{C^{\mathrm{def}}_{\mathrm{O}_3,i,j,l,t}}\Big|_t\right]}{a_1 b_2} \end{aligned} \tag{25}$$

The first-order, second-order, and cross-sensitivities computed by the hyperdual step method have been shown to be numerically exact for the hyperdualized elements of the model (Fike and Alonso, 2011; Liu et al., 2024). The first-order semi-normalized sensitivities are represented compactly as exemplified below

$$S^{\mathrm{O}_3}_{\mathrm{NO}_x} = \overline{\frac{\partial C_{\mathrm{O}_3,i,j,l=0,t}}{\partial E^{\mathrm{def}}_{\mathrm{NO}_x,\mathrm{dom}}}}\Bigg|_t E^{\mathrm{def}}_{\mathrm{NO}_x,\mathrm{dom}} \tag{26}$$

where $S^{\mathrm{O}_3}_{\mathrm{NO}_x}$ is the first-order semi-normalized sensitivity of first layer or ground level O_3 concentrations to NO_x emis-

sions, and the second-order semi-normalized sensitivity as

$$S^{(2)O_3}_{NO_x} = \left.\overline{\frac{\partial^2 C_{O_3,i,j,l=0,t}}{\partial E^{def}_{NO_x,dom}{}^2}}\right|_t \left(E^{def}_{NO_x,dom}\right)^2 \quad (27)$$

where $S^{(2)O_3}_{NO_x}$ is the second-order semi-normalized sensitivity of O_3 concentration to NO_x emissions.

3 Results and Discussion

3.1 Evaluation of sensitivities from GEOS-Chem-hyd

The implementation of GEOS-Chem-hyd was evaluated by comparing the first- and second- order semi-normalized sensitivities for a brief episode for a select set of concentrations with respect to emissions. Emissions of select species were perturbed domain-wide in hyperdual or real space for a 24 h model run, and the influences on surface level concentrations of select species were assessed.

The first-order, semi-normalized sensitivities from the hyperdual approach were compared with those from the central finite difference (FD) method. The first-order hyperdual sensitivities have robust agreement with the FD sensitivities when the relationship of the emissions to the concentration is expected to be linear such as for $S^{SO_2}_{SO_2}$, $S^{NO_2}_{NO_x}$, S^{ISOP}_{ISOP}, and $S^{OA_{bio}}_{ISOP}$ (Fig. 2, Table 1) as evidenced by the slopes and R^2 values of the linear regression of the two sets of sensitivities close to unity. The deviation from unity for some relationships expected to exhibit nonlinear behaviour (e.g., $S^{NH_4}_{SO_2}$, $S^{NH_3}_{SO_2}$, $S^{PM_{2.5}}_{NO_x}$, and $S^{OA_{bio}}_{NO_x}$) may be attributed to the nonlinearity of the relationship or the model state changing with the FD method in a manner not required in the hyperdual approach, such as regime switching between thermodynamic cases (Fig. S3). The level of agreement is similar to the first-order evaluation of CMAQ-hyd with the exception of much better agreement of the hyperdual and FD sensitivities for $S^{PM_{2.5}}_{SO_2}$ (Liu et al., 2024), which may be attributable to the smaller concentration gradients of SO_2 in the coarser model grid.

To illustrate the impact of the model state changing in the FD approach, the spatial difference in sensitivities between the FD and hyperdual of ground-level, time-averaged O_3 concentrations to the domain-wide emissions of NO_x are shown with different FD perturbation sizes (Fig. 3b–c). The results demonstrate clear consistency between the hyperdual and FD sensitivities at small perturbation sizes (105 %, 95 %) (Fig. 3a–b). However, as the perturbation size increases substantially (200 %, 0 %), the FD sensitivities increasingly deviate from the hyperdual, especially in chemically nonlinear regions such as East China (Fig. 3c). This divergence highlights the compounded effects of truncation errors and significant shifts in chemical regimes caused by large perturbations. Consequently, choosing an optimal perturbation size for FD calculations requires case-by-case adjustments tailored to specific species and chemical environments. On the contrary, the hyperdual method delivers accurate sensitivities without altering the model state.

Comparing $S^{O_3}_{NO_x}$ hyperdual sensitivities to the forward, central, and backward finite difference sensitivities following Henze et al. (2007) provides further insight into the accuracy of the augmented model (Fig. 4). The tight agreement of the hyperdual sensitivities with the three finite difference methods at a 5 % perturbation confirms the assessment of strong performance of the augmented model for this relationship (Fig. 4a). Worsening agreement with all FD methods with an increased perturbation size (100 %) (Fig. 4b) indicates a nonlinear model response. Additionally, these results align with the expectation that the central FD sensitivity should lie between the forward and backward FD sensitivities. For the $S^{PM_{2.5}}_{NO_x}$ (Fig. S4), the smaller perturbation results in consistent deviation from the one-to-one line for all three FD methods. With the larger perturbation, the backward and forward FD points usually bound the one-to-one line (Fig. S4b), which suggests that the hyperdual sensitivities are correct though the model state may differ with the real perturbation. Collectively, these results further demonstrate the validity of the first-order hyperdual sensitivities.

Evaluation of the second-order sensitivities from GEOS-Chem-hyd was conducted with the hybrid approach described in Sect. 2.3. Second-order sensitivities were evaluated through comparisons between GEOS-Chem-hyd and the hybrid methods using one-to-one plots (Fig. 5) as was done for CMAQ-hyd (Liu et al., 2024). The hybrid method reduces the sensitivity of the second-order sensitivities to perturbation sizes (Berman et al., 2023).

The statistics of the linear regression of the data in each subplot of Fig. 5 (Table 2) indicate that the agreement between hyperdual and hybrid sensitivities with respect to SO_2 are weak while those with respect to NO_x and ISOP are strong. As noted in Liu et al. (2024), the disagreement between the hybrid and hyperdual sensitivities for SO_2 is attributable to the dependence on FD within the hybrid method, which introduces disagreement in the first-order sensitivities with respect to SO_2 emissions (Fig. 2a–d). This disagreement is primarily due to the regime switching in the sulfate response (Fig. S3): ISORROPIA selects its equilibrium sub-case from the sulfate and sodium ratios, in which nitrate does not appear, so perturbing SO_2 emissions can place the base and perturbed states in different thermodynamic regimes while perturbing NO_x emissions affects the sub-case only indirectly. Where a regime boundary is crossed, the FD component of the hybrid estimator forms a difference quotient across a discontinuity in the solver response rather than a local curvature. Further analysis shows that the hybrid values are in fact less often negative than the hyperdual (52.5 % versus 63.8 % of cells; Fig. S5), with the one-sidedness apparent in Fig. 5c confined to the large-magnitude tail. These cells with the large differences from hyperdual occur in ar-

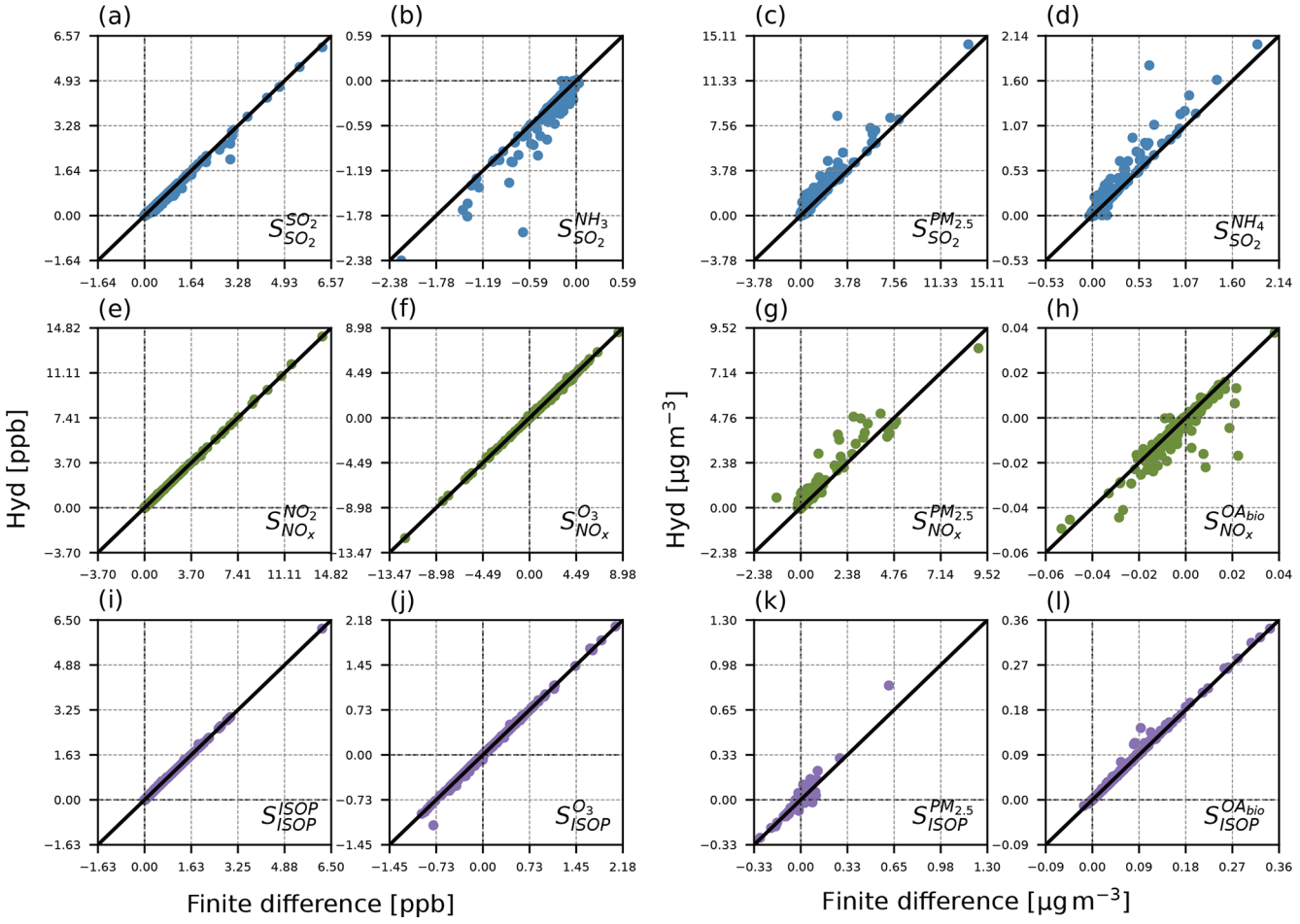

Figure 2. Comparisons of first-order semi-normalized sensitivities of the time-averaged concentration in each ground layer cell to the domain-wide emissions throughout the 24 h episode using the hyperdual step method (Hyd) and the central finite difference method with a 5 % perturbation in each direction. The sensitivity plots are polychromed by the domain-wide perturbed emissions of SO_2, NO_x, or isoprene (ISOP) as indicated in the subscript. The superscript indicates the concentration. The calculated sensitivities are labelled at the bottom right corner of each panel. The left two panels show examples of gas-phase species concentrations with respect to corresponding emissions. The right two panels show examples of aerosol-phase products with respect to their gaseous precursors.

Table 1. The slopes and R^2 values from the linear regression of the data in each subplot of Fig. 2 in the corresponding order.

First-order sensitivity: slope, R^2			
$S^{SO_2}_{SO_2}$: 0.96, 0.99	$S^{NH_3}_{SO_2}$: 1.17, 0.94	$S^{PM_{2.5}}_{SO_2}$: 1.14, 0.95	$S^{NH_4}_{SO_2}$: 1.17, 0.94
$S^{NO_2}_{NO_x}$: 1.00, 1.00	$S^{O_3}_{NO_x}$: 1.00, 1.00	$S^{PM_{2.5}}_{NO_x}$: 1.06, 0.92	$S^{OA_{bio}}_{NO_x}$: 0.96, 0.82
S^{ISOP}_{ISOP}: 1.00, 1.00	$S^{O_3}_{ISOP}$: 1.01, 1.00	$S^{PM_{2.5}}_{ISOP}$: 1.12, 0.93	$S^{OA_{bio}}_{ISOP}$: 1.02, 1.00

eas where point source SO_2 emissions (e.g., shipping, coal-fired power plants) are expected and are more likely to lead to regime changes influencing the $PM_{2.5}$ response when emissions are perturbed in a multiplicative manner (Fig. S6).

The agreement between the hyperdual and hybrid sensitivities is much stronger for second-order sensitivities with respect to NO_x and ISOP. The self-sensitivities, $S^{(2)NO_2}_{NO_x}$ and $S^{(2)ISOP}_{ISOP}$, show strong agreement, with slopes of 1.02 to 1.03, respectively, and both R^2 values being 1.00 (Table 2). Other gas-phase concentrations also show good agreement, consistent with nearly linear processes. The degree of agreement for $S^{(2)PM_{2.5}}_{NO_x}$ is slightly less than that for $S^{(2)NO_2}_{NO_x}$ and $S^{(2)O_3}_{NO_x}$, indicating more nonlinearity in the formation process from NO_x emissions to $PM_{2.5}$ concentrations. The $S^{(2)OA_{bio}}_{NO_x}$

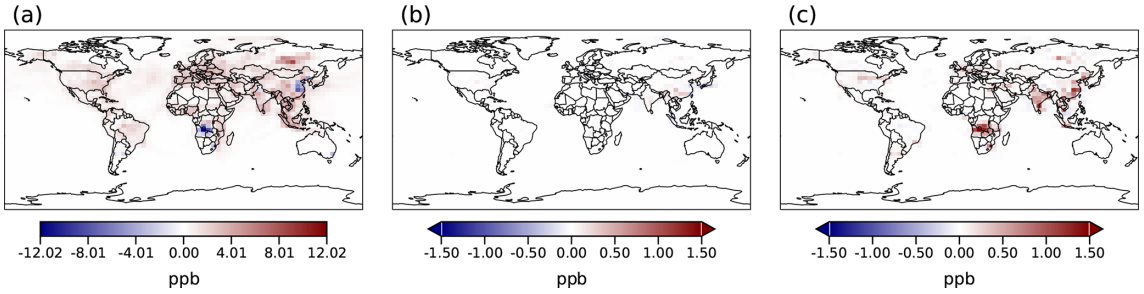

Figure 3. Map of **(a)** the first-order semi-normalized sensitivities of time-averaged, ground layer ozone concentrations with respect to domain-wide, persistent hyperdual perturbation of NO_x emissions. The differences between the 24 h average sensitivities from central finite difference (FD) and the hyperdual **(b)** when FD sensitivities are calculated with a 5 % perturbation in each direction (105 %, 95 %) and **(c)** when FD sensitivities are calculated with a 100 % perturbation in each direction (200 %, 0 %).

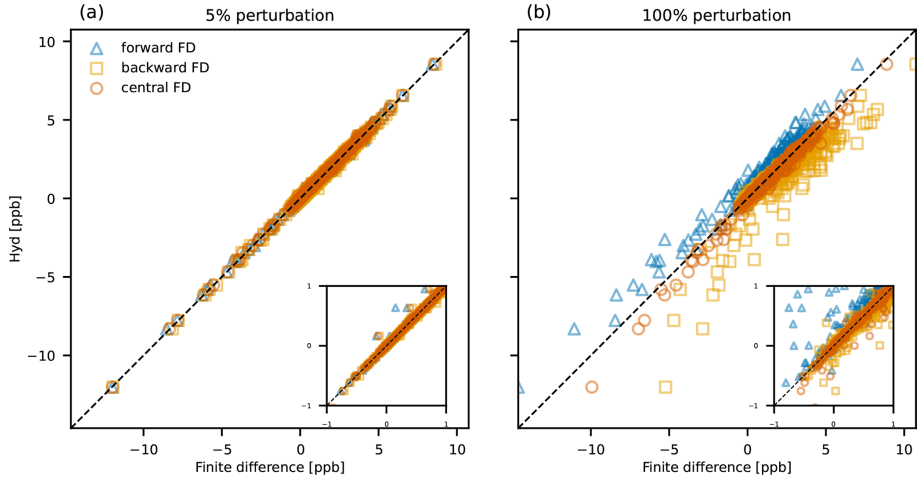

Figure 4. Comparison of first-order semi-normalized sensitivities of the time-averaged, ground layer ozone concentrations with respect to domain-wide, persistent perturbation of NO_x emissions throughout the 24 h episode using the hyperdual step method (Hyd) and various FD methods with a 5 % **(a)** and 100 % perturbation **(b)** in each direction.

relationship has a slope of 1.00 and an R^2 value of 0.93, indicating no proportional bias between the hyperdual and hybrid sensitivities but some scatter. To further investigate the impacts of model state changes and the inaccuracy inherent in the FD method, we analysed the spatial distribution of ground layer O_3concentrations to domain-wide perturbations of NO_x emissions (Fig. 6). Panels (b)–(d) illustrate the spatial differences between second-order sensitivities derived using the central FD method and the hyperdual approach. Subtractive cancellation errors significantly degrade sensitivity estimates for smaller perturbation sizes (105 %, 95 %), resulting in noisy and unreliable outcomes (Fig. 6b). Although larger perturbation sizes (150 %, 50 %; 200 %, 0 %) mitigate subtractive cancellation errors to some extent, noticeable truncation errors and unintended shifts in the model state persist (Fig. 6c–d). Consequently, the second-order central FD method becomes inaccurate and unsuitable for calculating derivatives within strongly nonlinear chemical systems. In contrast, the hyperdual method provides accurate second-order sensitivities without the susceptibility to subtractive cancellation or truncation errors, preserving the original model state throughout the calculation. This comparison demonstrates the value of the independence of the hyperdual sensitivity from perturbation-induced changes to the model state.

3.2 Computational cost of GEOS-Chem-hyd

We assessed the computational overhead of the augmented GEOS-Chem-hyd model through direct comparison with the standard "base" GEOS-Chem on the National Science Foundation-supported Derecho cluster using 128 CPU cores (Computational and Information Systems Laboratory, 2023). Both models were compiled in optimized "release" mode and executed for a 24 h simulation. Wall time for the entire model and each major process were determined via the built-in GEOS-Chem timers (Fig. 7). Hyperdual function calculations require 4–14 times that of a real function calculation (Fike and Alonso, 2011), which depends on the complexity

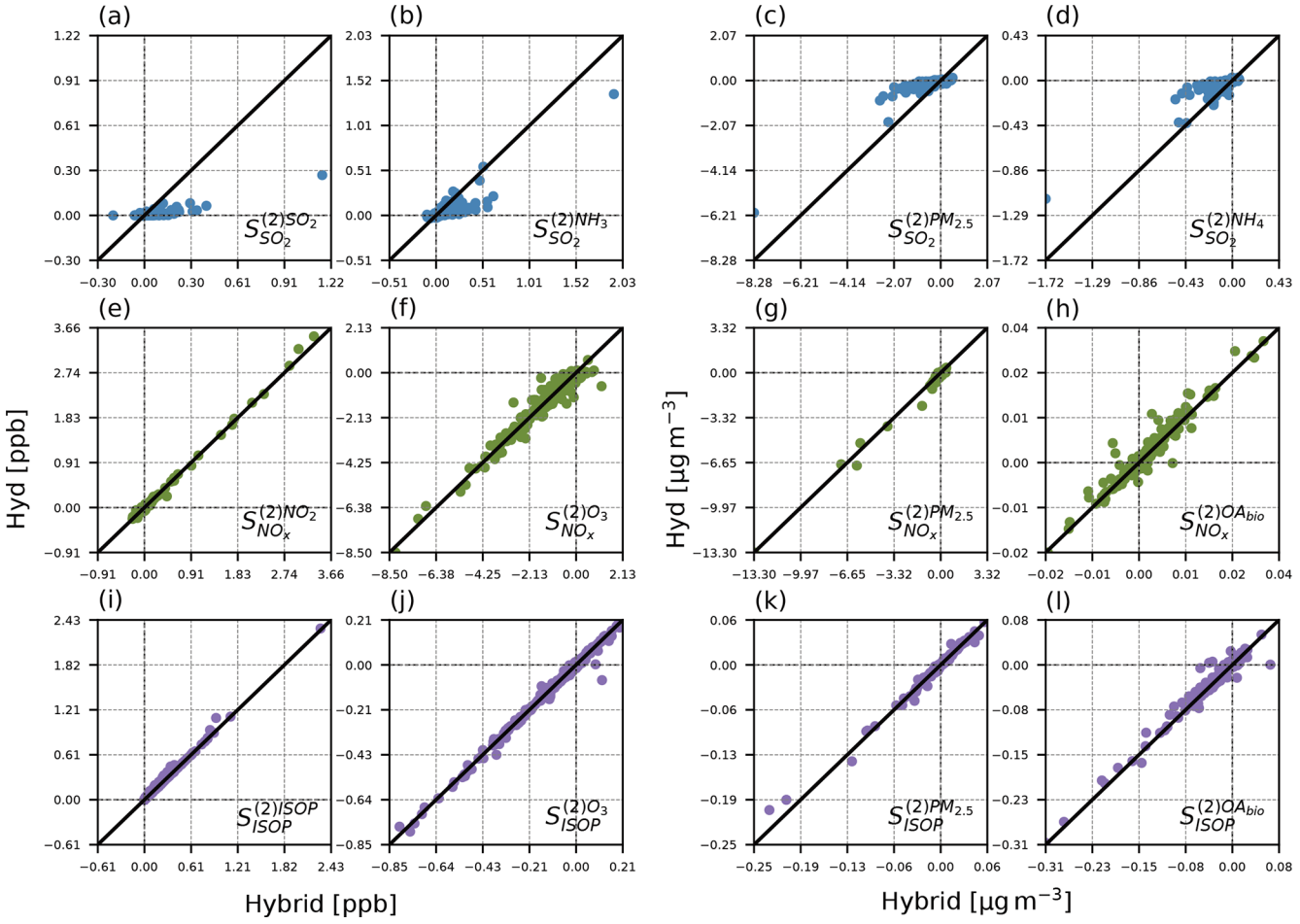

Figure 5. Comparisons of second-order semi-normalized sensitivities of the species indicated in the superscript in each ground layer cell averaged over the 24 h episode to domain-wide emissions of the species indicated in the subscript using the hyperdual step (Hyd) and the hybrid methods. The sensitivity plots are polychromed by the domain-wide perturbed emissions of SO_2, NO_x, or ISOP as indicated in the subscript. The calculated sensitivities are labelled in the bottom right corner of each panel. The left two panels show examples of gas-phase species concentrations with respect to corresponding emissions, while the right two panels show examples of aerosol-phase products with respect to their gaseous precursors.

Table 2. The slopes and R^2 values from the linear regression of the data in each subplot in Fig. 5 in the corresponding order.

Second-order sensitivity: slope, R^2			
$S^{(2)SO_2}_{SO_2}$: 0.18, 0.78	$S^{(2)NH_3}_{SO_2}$: 0.53, 0.78	$S^{(2)PM_{2.5}}_{SO_2}$: 0.50, 0.79	$S^{(2)NH_4}_{SO_2}$: 0.52, 0.80
$S^{(2)NO_2}_{NO_x}$: 1.02, 1.00	$S^{(2)O_3}_{NO_x}$: 0.98, 0.97	$S^{(2)PM_{2.5}}_{NO_x}$: 1.01, 0.99	$S^{(2)OA_{bio}}_{NO_x}$: 1.00, 0.93
$S^{(2)ISOP}_{ISOP}$: 1.03, 1.00	$S^{(2)O_3}_{ISOP}$: 1.00, 0.99	$S^{(2)PM_{2.5}}_{ISOP}$: 0.95, 0.99	$S^{(2)OA_{bio}}_{ISOP}$: 0.94, 0.97

of the function, the compiler behaviour, and the degree of optimization.

The total wall time for GEOS-Chem-hyd was approximately 3.9 times the cost of the base GEOS-Chem run (Fig. 7b). Since the FD approach would require three model runs without any tuning of the perturbation size, the computational cost of GEOS-Chem-hyd is competitive. The average memory usage for the base run was 10.6 GB while that for GEOS-Chem-hyd was 32.7 GB. Selective implementation of the hyperdual type provided some efficiency gains over the expected computational and memory increases. The hyperdualized gas phase chemistry and photolysis processes produces the largest relative increases in computational cost compared with the base model, at factors of 10.5 and 28.7, re-

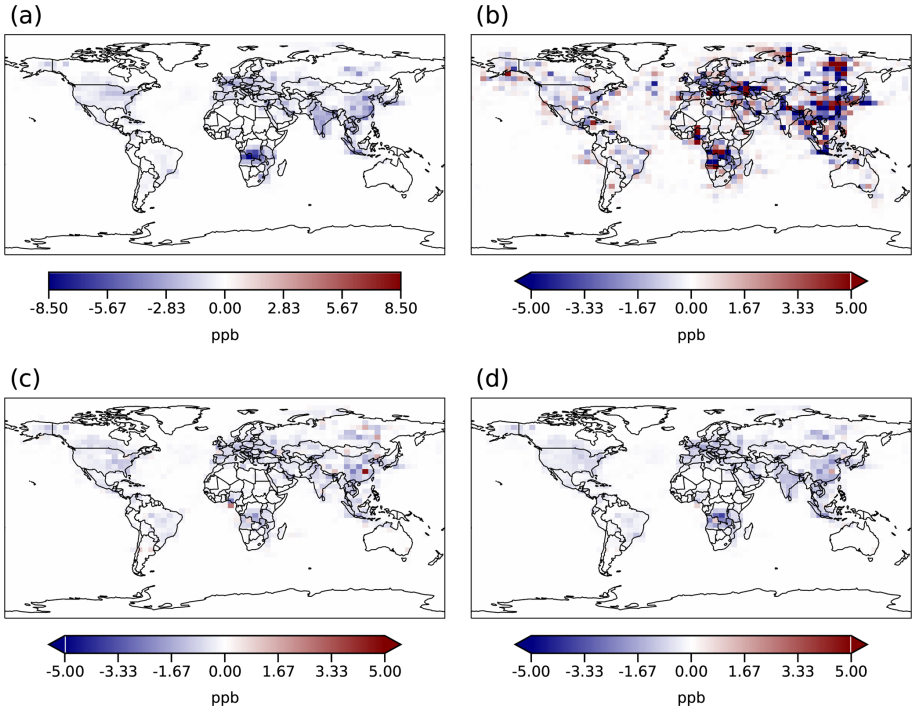

Figure 6. Map of the second-order semi-normalized sensitivities of ground layer ozone concentration averaged over the 24 h episode with respect to domain-wide hyperdual perturbation of NO_x emissions **(a)**. The differences between the 24 h average sensitivities from central finite difference (FD) and the hyperdual **(b)** when FD sensitivities are calculated with a 5 % perturbation in each direction (105 %, 95 %), **(c)** when FD sensitivities are calculated with a 50 % perturbation in each direction (150 %, 50 %) and **(d)** when FD sensitivities are calculated with a 100 % perturbation in each direction (200 %, 0 %).

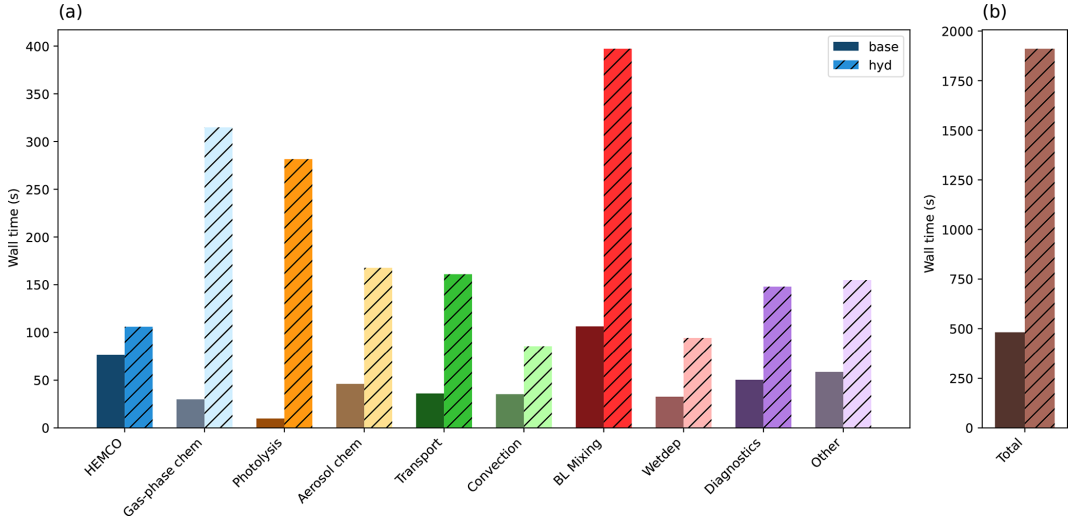

Figure 7. The computational time required for the base GEOS-Chem (left bar) in comparison to GEOS-Chem-hyd (right bar) in release mode. The wall time over a 24 h time-averaged simulation is shown on the y-axis, and relevant processes are shown on the x-axis. The wall time for each process is shown in **(a)** while the total wall time for each simulation is shown in **(b)**.

spectively (Fig. 7a). These processes include several nested loops, which may induce poor load balancing and extended computational tasks assigned to a single core. As expected, the least proportional change (1.4) occurred for the HEMCO model, which is not yet fully hyperdualized. The computational costs of other processes were comparable to those of the FD method, ranging from 2.3 to 4.2 times the same process in the base GEOS-Chem simulation.

3.3 Application of GEOS-Chem-hyd

To demonstrate the practical value of simultaneously calculating first- and second-order source-oriented sensitivities, the effects of domain-wide NO_x emissions on concentrations were quantified with a single GEOS-Chem-hyd simulation of 1–28 August 2019. The time-averaged, first- and second-order semi-normalized sensitivities of ground-layer O_3, $PM_{2.5}$, NH_4^+, and biogenic organic aerosol (OA_{bio}) concentrations to domain-wide NO_x emissions provide adequate information for assessing how a fractional change in domain-wide emissions would impact the concentrations in any ground layer grid cell (Fig. 8).

The first-order sensitivities of O_3 concentrations to domain-wide NO_x emissions, $S^{O_3}_{NO_x}$, are predominantly positive across most regions (Fig. 8a), indicating that an increase in domain-wide NO_x emissions will lead to an increase in O_3 concentrations with variation in the magnitude of the change. The second-order sensitivities, $S^{(2)O_3}_{NO_x}$, are predominantly negative (Fig. 8e), indicating a concave nonlinear relationship. Accordingly, first-order estimates alone would underestimate the influence of NO_x emission reductions on O_3 concentrations but overestimate the influence of NO_x emission increases on O_3 concentrations. For example, in the central-west region of Brazil (18° S, 60° W) where the first-order sensitivity is approximately 11 ppb, a 20 % reduction in domain-wide NO_x emissions would be predicted to lead to a reduction of O_3 concentrations by 2.2 ppb considering only the first-order sensitivity. However, including the second-order sensitivity of around −20 ppb adjusts this estimate for a 20 % reduction in domain-wide NO_x emissions to a more realistic O_3 concentration reduction of approximately 2.6 ppb. For highly nonlinear processes, approximating the influence of emissions controls requires considering these higher-order terms.

The first-order sensitivities of $PM_{2.5}$ to domain-wide NO_x emissions, $S^{PM_{2.5}}_{NO_x}$, are also predominantly positive (Fig. 8b). Over eastern China, the $S^{PM_{2.5}}_{NO_x}$ is largely positive, which indicates that an increase in domain-wide NO_x emissions will lead to an increase in $PM_{2.5}$concentrations in this region. However, $S^{(2)PM_{2.5}}_{NO_x}$ (Fig. 8f) are predominantly negative, implying an overestimation the response of $PM_{2.5}$ to domain-wide increases in NO_x emissions or an underestimation of the response to a decrease in emissions if neglecting the second-order term. The $S^{PM_{2.5}}_{NO_x}$ (Fig. 8b) and $S^{NH_4^+}_{NO_x}$ (Fig. 8c) have similar spatial patterns though the latter has a much smaller magnitude. $S^{NH_4^+}_{NO_x}$ indicate the extent to which domain-wide NO_x emissions lead to additional NH_4^+ in the aerosol, which is only a portion of the total $PM_{2.5}$. Like $S^{(2)PM_{2.5}}_{NO_x}$ (Fig. 8f), $S^{(2)NH_4^+}_{NO_x}$ (Fig. 8g) are predominantly negative.

The sensitivities of OA_{bio} to domain-wide NO_x emissions, $S^{OA_{bio}}_{NO_x}$, exhibit significant regional variability. Secondary organic aerosols (SOA) formed from isoprene and terpene oxidation constitute the OA_{bio} in GEOS-Chem. Sensitivities of OA_{bio} to NO_x differ regionally. Over the continental US, Mexico, central Africa, Europe, China, and western Asia, the $S^{OA_{bio}}_{NO_x}$ (Fig. 8d) is primarily negative, which indicates that increasing domain-wide NO_xemissions would suppress OA_{bio} formation. In boreal eastern Russia, the $S^{OA_{bio}}_{NO_x}$ is slightly positive. This contrast arises from differences in volatile organic compound precursors, oxidant chemistry, meteorology, and land cover. Boreal conifer forests emit mainly monoterpenes (e.g., α-pinene), which are oxidized by nitrate radicals (NO_3) and OH to produce low-volatility organonitrates. Laboratory and field studies show that NO_3 reacting with monoterpenes yields aerosol organonitrates (23 %–44 %) (Ayres et al., 2015). Thus, in regions like eastern Siberia with abundant monoterpenes and seasonally strong NO_3, adding NO_x boosts OA_{bio} via organonitrates. By contrast, in high-NO_x, isoprene-rich regions (e.g., SE US during daytime, urban plumes), NO_x may suppress OA_{bio} formation through reduction of IEPOX-derived SOA and increased volatile nitrate formation (De Sá et al., 2017; Zhang et al., 2017). In summary, NO_x may enhance OA_{bio} formation where organonitrate pathways dominate (typically cooler, NO_x-limited/monoterpene areas) but can inhibit SOA where high-NO_x truncates IEPOX or OH-driven yields (warmer, VOC-rich areas). These dynamics are evident in the sensitivities from this simulation. The inhibition caused by high-NO_x can be seen in more industrial regions in the Eastern US, where there is a larger negative $S^{OA_{bio}}_{NO_x}$ compared to other regions in the country (Fig. 8d). The second-order sensitivities tend to oppose the signal of the first-order sensitivity. Generally, in regions with positive $S^{(2)OA_{bio}}_{NO_x}$ (Fig. 8h), the $S^{OA_{bio}}_{NO_x}$ is negative and vice versa. In select places like eastern China and central Peru, the negative $S^{(2)OA_{bio}}_{NO_x}$ (Fig. 8h) is much greater in magnitude than the positive $S^{OA_{bio}}_{NO_x}$ (Fig. 8d), which indicates significant nonlinearity. For example, in the southern portion of Hebei, China (38° N, 115° E), the $S^{OA_{bio}}_{NO_x}$ is $+0.018\,\mu g\,m^{-3}$ while the $S^{(2)OA_{bio}}_{NO_x}$ is $-0.094\,\mu g\,m^{-3}$. Because of the opposing signs of the derivatives and the difference in their magnitudes, an increase in emissions greater than 38 % shifts from a corresponding increase in OA_{bio} concentrations to a decrease. For example, a 50 % increase in domain-wide NO_x emissions would be predicted to result in a local $0.009\,\mu g\,m^{-3}$ increase considering only the first-order

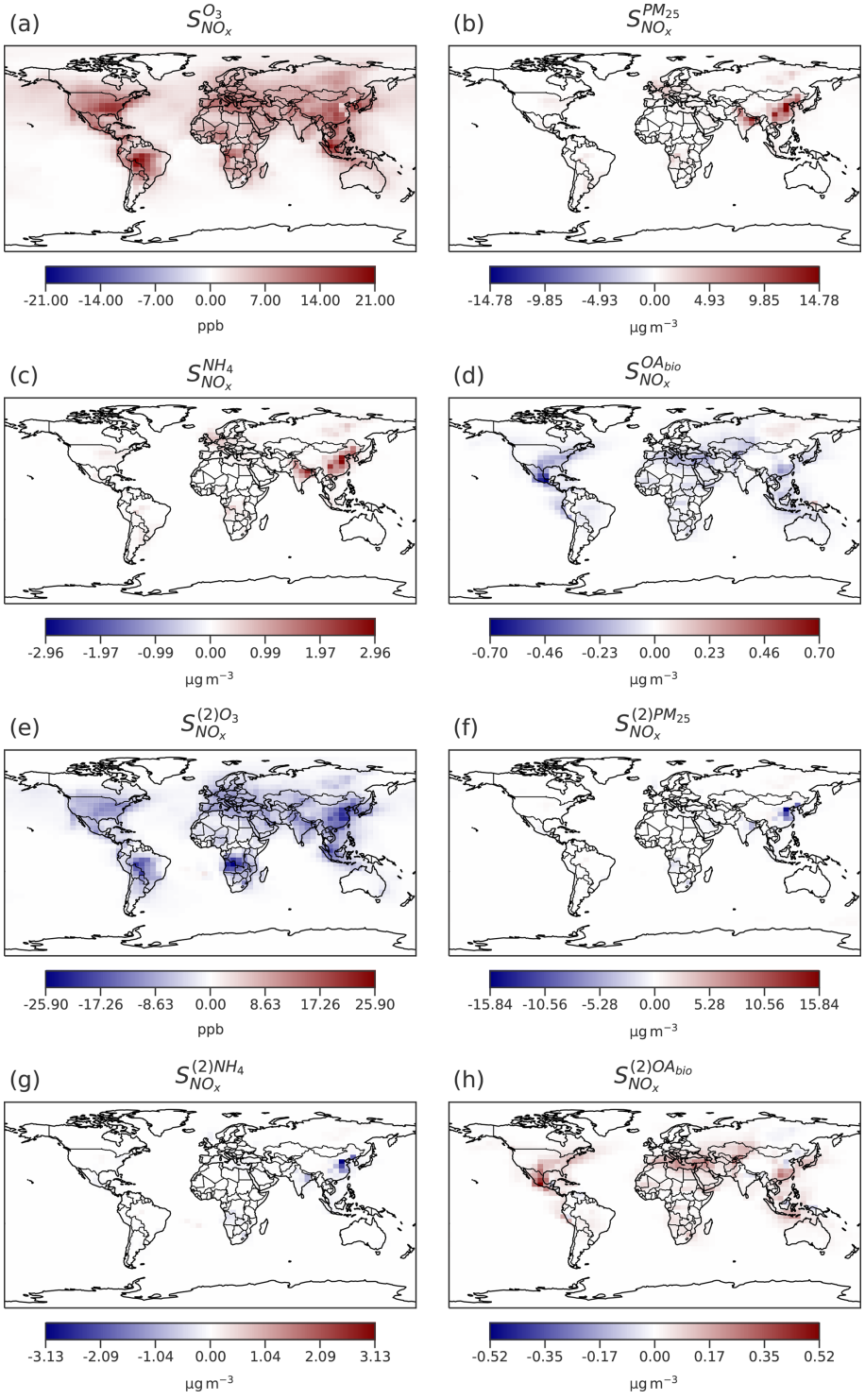

Figure 8. First- and second-order semi-normalized sensitivities of time-averaged O_3, $PM_{2.5}$, NH_4^+, and OA_{bio} concentrations with respect to NO_x emissions on the ground layer for a 4-week simulation. Panels **(a)**–**(d)** show the first-order sensitivities and **(e)**–**(h)** show the second-order sensitivities.

term but a $0.003\,\mu g\,m^{-3}$ decrease considering the first- and second-order terms.

We also conducted one-week simulations for the first week of February, May, and November of 2019, to confirm the stability of the GEOS-Chem-hyd sensitivity calculations across different model states (Fig. S7). The time-averaged $S_{NO_x}^{PM_{2.5}}$ and $S_{NO_x}^{(2)PM_{2.5}}$ demonstrate that seasonality affects the influence of NO_x emissions on $PM_{2.5}$ concentrations especially in the northern hemisphere and in South Asia (Fig. S7). The addition of accurate second-order sensitivities can help researchers and environmental decisionmakers develop more accurate emission control strategies for pollutants such as O_3 and $PM_{2.5}$ that respond nonlinearly to precursor emissions.

4 Conclusion

We implemented the hyperdual step method in GEOS-Chem to create GEOS-Chem-hyd. This augmented model computes numerically exact first- and second-order sensitivities in a single model execution. GEOS-Chem-hyd provides a robust alternative to existing numerical methods, overcoming limitations such as subtractive cancellation and truncation errors inherent in the finite difference method. Moreover, it complements the GEOS-Chem adjoint by efficiently addressing source-oriented sensitivities and nonlinear interactions.

The evaluations demonstrated robust agreement between GEOS-Chem-hyd and established methods. First-order sensitivity comparisons with the central finite difference method showed strong alignment, particularly for linear relationships. Second-order sensitivities of nonlinear processes are difficult to evaluate so a hybrid hyperdual-central finite difference method was employed. GEOS-Chem-hyd exhibits a smaller spread, whereas finite difference methods demonstrated dependence on the size of the real perturbation and subsequent model state.

GEOS-Chem-hyd was applied to understand the influence of domain-wide NO_x emissions on the concentrations in each ground-level grid cell of O_3, $PM_{2.5}$, NH_4^+, and OA_{bio}. The second-order sensitivities shift the response expected from the first-order sensitivity alone. For the OA_{bio}, the sensitivities varied regionally. For example, the NO_x-induced formation of OA_{bio} showed contrasting regional responses dependent on precursor chemistry, oxidant availability, and meteorological conditions. In short, this application demonstrates that GEOS-Chem-hyd may provide insights for environmental decisionmakers seeking to optimize emission reduction strategies or scientists estimating the influence of an emission source on pollutants.

The computational cost of GEOS-Chem-hyd is approximately four times that of the base model. Strategic variable conversion limited the overhead associated with hyperdual calculations. Accordingly, GEOS-Chem-hyd is competitive with existing sensitivity analysis methods. Future work includes fully integrating the hyperdual method within the HEMCO for sector-specific applications. Longer simulations in GEOS-Chem-hyd are fully supported and can be explored in future scientific applications as computational resources permit. In future work, the framework could also be extended to the high-performance configuration of GCHP (Eastham et al., 2018; Martin et al., 2022). Specialized configurations, such as the TOMAS aerosol microphysics scheme, are likewise not yet supported.

Overall, GEOS-Chem-hyd represents a substantial advancement for atmospheric sensitivity analysis in a widely used global CTM, offering precise insights into pollutant dynamics in a computationally feasible manner. GEOS-Chem developers may also find this augmented version useful for debugging the implementation of new code or for assessing the impact of a scientific advancement newly implemented in the model. Accurate second-order sensitivities computed by GEOS-Chem-hyd are valuable for understanding complex atmospheric chemistry interactions and improving the effectiveness of policy interventions aimed at mitigating air pollution impacts.

Code and data availability. The hyperdual implementation is of GEOS-Chem Classic version 14.0.0-rc.3, which is available at https://github.com/geoschem/geos-chem/releases/tag/14.0.0-rc.3 (last access: 16 November 2026), coupled with HEMCO 3.5.0. The science codebase of this pre-release is identical to the released version 14.0.0 and is archived at https://doi.org/10.5281/zenodo.7254984 (The International GEOS-Chem User Community, 2022); the two differ only in the changelog, run-directory templates, and run-directory creation script. GEOS-Chem-hyd is archived at https://doi.org/10.5281/zenodo.16575027 (Akinjole et al., 2026a). Both the GEOS-Chem and the GEOS-Chem-hyd models are under MIT licenses. The input data configuration for the simulation experiments is available at https://doi.org/10.5281/zenodo.22699829 (Akinjole et al., 2026b).

Supplement. The supplement related to this article is available online at https://doi.org/10.5194/gmd-19-11243-2026-supplement.

Author contributions. SLC conceived of the idea and designed the model development. SOA developed the model code, performed the simulations, and developed the figures with direction from SLC. JL led the standalone ISORROPIA testing. SOA and SLC drafted the manuscript, which JL improved.

Competing interests. The contact author has declared that none of the authors has any competing interests.

Disclaimer. Publisher's note: Copernicus Publications remains neutral with regard to jurisdictional claims made in the text, published maps, institutional affiliations, or any other geographical representation in this paper. The authors bear the ultimate responsibil-

ity for providing appropriate place names. Views expressed in the text are those of the authors and do not necessarily reflect the views of the publisher.

Acknowledgements. The authors would like to acknowledge high-performance computing support from the Derecho system (https://doi.org/10.5065/qx9a-pg09) provided by the NSF National Center for Atmospheric Research (NCAR), sponsored by the National Science Foundation. The authors would also like to thank Dr. Ryan P. Russell for kindly providing the testing framework of multicomplex numbers, which inspired the development of the testing framework for hyperdual numbers, and Dr. Sebastian D. Eastham, who created the standalone framework that was used for testing ISORROPIA-hyd.

Financial support. The work of Samuel O. Akinjole, Jiachen Liu, and Shannon L. Capps was supported by National Science Foundation CAREER Award grant no. 1944669 to Shannon L. Capps. Samuel O. Akinjole was also supported by the NASA FINESST grant no. 80NSSC25K0399.

Review statement. This paper was edited by Volker Grewe and reviewed by two anonymous referees.

References

Akinjole, S. O., Capps, S., and Liu, J.: GEOS-Chem-14.0.0-hyd (1.1.0), Zenodo [code], https://doi.org/10.5281/zenodo.16575027, 2026a.

Akinjole, S. O., Capps, S., and Liu, J.: GEOS-Chem-14.0.0-hyd: simulation configurations and restart files (v1), Zenodo [data set], https://doi.org/10.5281/zenodo.22699829, 2026b.

Alexe, M. and Sandu, A.: On the discrete adjoints of adaptive time stepping algorithms, J. Comput. Appl. Math., 233, 1005–1020, https://doi.org/10.1016/j.cam.2009.08.109, 2009.

Anenberg, S. C., Miller, J., Henze, D. K., Minjares, R., and Achakulwisut, P.: The global burden of transportation tailpipe emissions on air pollution-related mortality in 2010 and 2015, Environ. Res. Lett., 14, 12, https://doi.org/10.1088/1748-9326/ab35fc, 2019.

Ayres, B. R., Allen, H. M., Draper, D. C., Brown, S. S., Wild, R. J., Jimenez, J. L., Day, D. A., Campuzano-Jost, P., Hu, W., de Gouw, J., Koss, A., Cohen, R. C., Duffey, K. C., Romer, P., Baumann, K., Edgerton, E., Takahama, S., Thornton, J. A., Lee, B. H., Lopez-Hilfiker, F. D., Mohr, C., Wennberg, P. O., Nguyen, T. B., Teng, A., Goldstein, A. H., Olson, K., and Fry, J. L.: Organic nitrate aerosol formation via NO_3^+ biogenic volatile organic compounds in the southeastern United States, Atmos. Chem. Phys., 15, 13377–13392, https://doi.org/10.5194/acp-15-13377-2015, 2015.

Belis, C. A., Pirovano, G., Villani, M. G., Calori, G., Pepe, N., and Putaud, J. P.: Comparison of source apportionment approaches and analysis of non-linearity in a real case model application, Geosci. Model Dev., 14, 4731–4750, https://doi.org/10.5194/gmd-14-4731-2021, 2021.

Berman, B., Capps, S. L., Sauvageau, I., Gao, E., Eastham, S. D., and Russell, R. P.: ISORROPIA-MCX: Enabling Sensitivity Analysis With Multicomplex Variables in the Aerosol Thermodynamic Model, ISORROPIA, Earth Space Sci., 10, e2022EA002729, https://doi.org/10.1029/2022EA002729, 2023.

Bey, I., Jacob, D. J., Yantosca, R. M., Logan, J. A., Field, B. D., Fiore, A. M., Li, Q. B., Liu, H. G. Y., Mickley, L. J., and Schultz, M. G.: Global modeling of tropospheric chemistry with assimilated meteorology: Model description and evaluation, J. Geophys. Res.-Atmos., 106, 23073–23095, https://doi.org/10.1029/2001jd000807, 2001.

Burnett, R. T., Pope, C. A., Ezzati, M., Olives, C., Lim, S. S., Mehta, S., Shin, H. H., Singh, G., Hubbell, B., Brauer, M., Anderson, H. R., Smith, K. R., Balmes, J. R., Bruce, N. G., Kan, H., Laden, F., Prüss-Ustün, A., Turner, M. C., Gapstur, S. M., Diver, W. R., and Cohen, A.: An Integrated Risk Function for Estimating the Global Burden of Disease Attributable to Ambient Fine Particulate Matter Exposure, Environ. Health Persp., 122, 397–403, https://doi.org/10.1289/ehp.1307049, 2014.

Butler, T., Lupascu, A., Coates, J., and Zhu, S.: TOAST 1.0: Tropospheric Ozone Attribution of Sources with Tagging for CESM 1.2.2, Geosci. Model Dev., 11, 2825–2840, https://doi.org/10.5194/gmd-11-2825-2018, 2018.

Capps, S. L., Hu, Y., and Russell, A. G.: Assessing Near-Field and Downwind Impacts of Reactivity-Based Substitutions, J. Air Waste Manage., 60, 316–327, https://doi.org/10.3155/1047-3289.60.3.316, 2010.

Capps, S. L., Henze, D. K., Hakami, A., Russell, A. G., and Nenes, A.: ANISORROPIA: the adjoint of the aerosol thermodynamic model ISORROPIA, Atmos. Chem. Phys., 12, 527–543, https://doi.org/10.5194/acp-12-527-2012, 2012.

Chen, Y., Shen, H., Kaiser, J., Hu, Y., Capps, S. L., Zhao, S., Hakami, A., Shih, J.-S., Pavur, G. K., Turner, M. D., Henze, D. K., Resler, J., Nenes, A., Napelenok, S. L., Bash, J. O., Fahey, K. M., Carmichael, G. R., Chai, T., Clarisse, L., Coheur, P.-F., Van Damme, M., and Russell, A. G.: High-resolution hybrid inversion of IASI ammonia columns to constrain US ammonia emissions using the CMAQ adjoint model, Atmos. Chem. Phys., 21, 2067–2082, https://doi.org/10.5194/acp-21-2067-2021, 2021.

Choi, J., Henze, D. K., Cao, H. S., Nowlan, C. R., Abad, G. G., Kwon, H. A., Lee, H. M., Oak, Y. J., Park, R. J., Bates, K. H., Maasakkers, J. D., Wisthaler, A., and Weinheimer, A. J.: An Inversion Framework for Optimizing Non-Methane VOC Emissions Using Remote Sensing and Airborne Observations in Northeast Asia During the KORUS-AQ Field Campaign, J. Geophys. Res.-Atmos., 127, 27, https://doi.org/10.1029/2021jd035844, 2022.

Cohan, D. S., Hakami, A., Hu, Y., and Russell, A. G.: Nonlinear response of ozone to emissions: source apportionment and sensitivity analysis, Environ. Sci. Technol., 39, 6739–6748, https://doi.org/10.1021/es048664m, 2005.

Computational and Information Systems Laboratory: Derecho: HPE Cray EX System (University Community Computing), NSF National Center for Atmospheric Research, Boulder, CO, https://doi.org/10.5065/qx9a-pg09, 2023.

Constantin, B. V. and Barrett, S. R. H.: Application of the complex step method to chemistry-transport modeling, Atmos. Environ., 99, 457–465, https://doi.org/10.1016/j.atmosenv.2014.10.017, 2014.

Cooper, M., Martin, R. V., Padmanabhan, A., and Henze, D. K.: Comparing mass balance and adjoint methods for inverse modeling of nitrogen dioxide columns for global nitrogen oxide emissions, J. Geophys. Res.-Atmos., 122, 4718–4734, https://doi.org/10.1002/2016jd025985, 2017.

de Sá, S. S., Palm, B. B., Campuzano-Jost, P., Day, D. A., Newburn, M. K., Hu, W., Isaacman-VanWertz, G., Yee, L. D., Thalman, R., Brito, J., Carbone, S., Artaxo, P., Goldstein, A. H., Manzi, A. O., Souza, R. A. F., Mei, F., Shilling, J. E., Springston, S. R., Wang, J., Surratt, J. D., Alexander, M. L., Jimenez, J. L., and Martin, S. T.: Influence of urban pollution on the production of organic particulate matter from isoprene epoxydiols in central Amazonia, Atmos. Chem. Phys., 17, 6611–6629, https://doi.org/10.5194/acp-17-6611-2017, 2017.

Ding, D., Xing, J., Wang, S. X., Liu, K. Y., and Hao, J. M.: Estimated Contributions of Emissions Controls, Meteorological Factors, Population Growth, and Changes in Baseline Mortality to Reductions in Ambient $PM_{2.5}$ and $PM_{2.5}$-Related Mortality in China, 2013–2017, Environ. Health Persp., 127, 12, https://doi.org/10.1289/ehp4157, 2019.

Dunker, A. M.: The decoupled direct method for calculating sensitivity coefficients in chemical kinetics, J. Chem. Phys., 81, 2385–2393, https://doi.org/10.1063/1.447938, 1984.

Dunker, A. M., Yarwood, G., Ortmann, J. P., and Wilson, G. M.: The Decoupled Direct Method for Sensitivity Analysis in a Three-Dimensional Air Quality Model Implementation, Accuracy, and Efficiency, Environ. Sci. Technol., 36, 2965–2976, https://doi.org/10.1021/es0112691, 2002a.

Dunker, A. M., Yarwood, G., Ortmann, J. P., and Wilson, G. M.: Comparison of source apportionment and source sensitivity of ozone in a three-dimensional air quality model, Environ. Sci. Technol., 36, 2953–2964, https://doi.org/10.1021/es011418f, 2002b.

Eastham, S. D., Weisenstein, D. K., and Barrett, S. R. H.: Development and evaluation of the unified tropospheric–stratospheric chemistry extension (UCX) for the global chemistry-transport model GEOS-Chem, Atmos. Environ., 89, 52–63, https://doi.org/10.1016/j.atmosenv.2014.02.001, 2014.

Eastham, S. D., Long, M. S., Keller, C. A., Lundgren, E., Yantosca, R. M., Zhuang, J., Li, C., Lee, C. J., Yannetti, M., Auer, B. M., Clune, T. L., Kouatchou, J., Putman, W. M., Thompson, M. A., Trayanov, A. L., Molod, A. M., Martin, R. V., and Jacob, D. J.: GEOS-Chem High Performance (GCHP v11-02c): a next-generation implementation of the GEOS-Chem chemical transport model for massively parallel applications, Geosci. Model Dev., 11, 2941–2953, https://doi.org/10.5194/gmd-11-2941-2018, 2018.

Elbern, H., Schwinger, J., and Botchorishvili, R.: Chemical state estimation for the middle atmosphere by four-dimensional variational data assimilation: System configuration, J. Geophys. Res.-Atmos., 115, 23, https://doi.org/10.1029/2009jd011953, 2010.

Emmons, L. K., Hess, P. G., Lamarque, J.-F., and Pfister, G. G.: Tagged ozone mechanism for MOZART-4, CAM-chem and other chemical transport models, Geosci. Model Dev., 5, 1531–1542, https://doi.org/10.5194/gmd-5-1531-2012, 2012.

Errico, R. M.: What Is an Adjoint Model?, B. Am. Meteorol. Soc., 78, 2577–2591, https://doi.org/10.1175/1520-0477(1997)078<2577:wiaam>2.0.co;2, 1997.

Fike, J. A. and Alonso, J. J.: The Development of Hyper-Dual Numbers for Exact Second-Derivative Calculations, 49th AIAA Aerospace Sciences Meeting including the New Horizons Forum and Aerospace Exposition, Orlando, Florida, 4–7 January 2011, https://doi.org/10.2514/6.2011-886, 2011.

Fisher, J. A., Murray, L. T., Jones, D. B. A., and Deutscher, N. M.: Improved method for linear carbon monoxide simulation and source attribution in atmospheric chemistry models illustrated using GEOS-Chem v9, Geosci. Model Dev., 10, 4129–4144, https://doi.org/10.5194/gmd-10-4129-2017, 2017.

Fountoukis, C. and Nenes, A.: ISORROPIA II: a computationally efficient thermodynamic equilibrium model for K^+-Ca^{2+}-Mg^{2+}-NH_4^+-Na^+-SO_4^{2-}-NO_3^--Cl^--H_2O aerosols, Atmos. Chem. Phys., 7, 4639–4659, https://doi.org/10.5194/acp-7-4639-2007, 2007.

Gelaro, R., McCarty, W., Suárez, M. J., Todling, R., Molod, A., Takacs, L., Randles, C. A., Darmenov, A., Bosilovich, M. G., Reichle, R., Wargan, K., Coy, L., Cullather, R., Draper, C., Akella, S., Buchard, V., Conaty, A., da Silva, A. M., Gu, W., Kim, G.-K., Koster, R., Lucchesi, R., Merkova, D., Nielsen, J. E., Partyka, G., Pawson, S., Putman, W., Rienecker, M., Schubert, S. D., Sienkiewicz, M., and Zhao, B.: The Modern-Era Retrospective Analysis for Research and Applications, Version 2 (MERRA-2), J. Climate, 30, 5419–5454, https://doi.org/10.1175/JCLI-D-16-0758.1, 2017.

Giering, R. and Kaminski, T.: Recipes for adjoint code construction, ACM T. Math. Software, 24, 437–474, https://doi.org/10.1145/293686.293695, 1998.

Giles, M. B. and Pierce, N. A.: An Introduction to the Adjoint Approach to Design, Flow Turbul. Combust., 65, 393–415, https://doi.org/10.1023/A:1011430410075, 2000.

Global Burden of Disease Collaborative Network: Global Burden of Disease Study 2023 (GBD 2023), Institute for Health Metrics and Evaluation (IHME), Seattle, United States, 2025.

Grewe, V., Tsati, E., and Hoor, P.: On the attribution of contributions of atmospheric trace gases to emissions in atmospheric model applications, Geosci. Model Dev., 3, 487–499, https://doi.org/10.5194/gmd-3-487-2010, 2010.

Griewank, A. and Walther, A.: Evaluating Derivatives: Principles and Techniques of Algorithmic Differentiation, 2nd Edn., Society for Industrial and Applied Mathematics, https://doi.org/10.1137/1.9780898717761, 2008.

Hakami, A., Odman, M. T., and Russell, A. G.: High-order, direct sensitivity analysis of multidimensional air quality models, Environ. Sci. Technol., 37, 2442–2452, https://doi.org/10.1021/es020677h, 2003.

Hakami, A., Odman, M. T., and Russell, A. G.: Nonlinearity in atmospheric response: A direct sensitivity analysis approach, J. Geophys. Res.-Atmos., 109, https://doi.org/10.1029/2003JD004502, 2004.

Han, H., Liu, J., Yuan, H., Wang, T., Zhuang, B., and Zhang, X.: Foreign influences on tropospheric ozone over East Asia through global atmospheric transport, Atmos. Chem. Phys., 19, 12495–12514, https://doi.org/10.5194/acp-19-12495-2019, 2019.

Hascoet, L. and Pascual, V.: The Tapenade automatic differentiation tool: Principles, model, and specification, ACM T. Math. Software, 39, 20, https://doi.org/10.1145/2450153.2450158, 2013.

Hascoët, L. and Dauvergne, B.: Adjoints of large simulation codes through Automatic Differentiation, Eur. J. Comput. Mech., 17, 63–86, https://doi.org/10.3166/remn.17.63-86, 2008.

Heimbach, P., Hill, C., and Giering, R.: An efficient exact adjoint of the parallel MIT General Circulation Model, generated via automatic differentiation, Future Gener. Comp. Sy., 21, 1356–1371, https://doi.org/10.1016/j.future.2004.11.010, 2005.

Henze, D. K., Hakami, A., and Seinfeld, J. H.: Development of the adjoint of GEOS-Chem, Atmos. Chem. Phys., 7, 2413–2433, https://doi.org/10.5194/acp-7-2413-2007, 2007.

Henze, D. K., Seinfeld, J. H., and Shindell, D. T.: Inverse modeling and mapping US air quality influences of inorganic $PM_{2.5}$ precursor emissions using the adjoint of GEOS-Chem, Atmos. Chem. Phys., 9, 5877–5903, https://doi.org/10.5194/acp-9-5877-2009, 2009.

Ikeda, K., Tanimoto, H., Sugita, T., Akiyoshi, H., Kanaya, Y., Zhu, C., and Taketani, F.: Tagged tracer simulations of black carbon in the Arctic: transport, source contributions, and budget, Atmos. Chem. Phys., 17, 10515–10533, https://doi.org/10.5194/acp-17-10515-2017, 2017.

Jaeglé, L., Shah, V., Thornton, J. A., Lopez-Hilfiker, F. D., Lee, B. H., McDuffie, E. E., Fibiger, D., Brown, S. S., Veres, P., Sparks, T. L., Ebben, C. J., Wooldridge, P. J., Kenagy, H. S., Cohen, R. C., Weinheimer, A. J., Campos, T. L., Montzka, D. D., DiGangi, J. P., Wolfe, G. M., Hanisco, T., Schroder, J. C., Campuzano-Jost, P., Day, D. A., Jimenez, J. L., Sullivan, A. P., Guo, H., and Weber, R. J.: Nitrogen Oxides Emissions, Chemistry, Deposition, and Export Over the Northeast United States During the WINTER Aircraft Campaign, J. Geophys. Res.-Atmos., 123, 12368–12393, https://doi.org/10.1029/2018jd029133, 2018.

Keller, C. A., Evans, M. J., Knowland, K. E., Hasenkopf, C. A., Modekurty, S., Lucchesi, R. A., Oda, T., Franca, B. B., Mandarino, F. C., Díaz Suárez, M. V., Ryan, R. G., Fakes, L. H., and Pawson, S.: Global impact of COVID-19 restrictions on the surface concentrations of nitrogen dioxide and ozone, Atmos. Chem. Phys., 21, 3555–3592, https://doi.org/10.5194/acp-21-3555-2021, 2021.

Kharol, S. K., Martin, R. V., Philip, S., Vogel, S., Henze, D. K., Chen, D., Wang, Y., Zhang, Q., and Heald, C. L.: Persistent sensitivity of Asian aerosol to emissions of nitrogen oxides, Geophys. Res. Lett., 40, 1021–1026, https://doi.org/10.1002/grl.50234, 2013.

Kim, S. Y., Lee, S. D., Lee, J. B., Kim, D. R., Han, J. S., Choi, K. H., and Song, C. K.: Analysis of Long-Range Transport of Carbon Dioxide and Its High Concentration Events over East Asian Region Using GOSAT Data and GEOS-Chem Modeling, Adv. Meteorol., 2015, 13, https://doi.org/10.1155/2015/680264, 2015.

Kleeman, M. J. and Cass, G. R.: A 3D Eulerian Source-Oriented Model for an Externally Mixed Aerosol, Environ. Sci. Technol., 35, 4834–4848, https://doi.org/10.1021/es010886m, 2001.

Koo, B., Dunker, A. M., and Yarwood, G.: Implementing the decoupled direct method for sensitivity analysis in a particulate matter air quality model, Environ. Sci. Technol., 41, 2847–2854, https://doi.org/10.1021/es0619962, 2007.

Lantoine, G., Russell, R. P., and Dargent, T.: Using Multicomplex Variables for Automatic Computation of High-Order Derivatives, ACM T. Math. Software, 38, 1–21, https://doi.org/10.1145/2168773.2168774, 2012.

Lapina, K., Henze, D. K., Milford, J. B., Huang, M., Lin, M., Fiore, A. M., Carmichael, G., Pfister, G. G., and Bowman, K.: Assessment of source contributions to seasonal vegetative exposure to ozone in the U.S, J. Geophys. Res.-Atmos., 119, 324–340, https://doi.org/10.1002/2013jd020905, 2014.

Le, T. H., Wang, Y., Liu, L., Yang, J. N., Yung, Y. L., Li, G. H., and Seinfeld, J. H.: Unexpected air pollution with marked emission reductions during the COVID-19 outbreak in China, Science, 369, 702–706, https://doi.org/10.1126/science.abb7431, 2020.

Li, C., Martin, R. V., Shephard, M. W., Cady-Pereira, K., Cooper, M. J., Kaiser, J., Lee, C. J., Zhang, L., and Henze, D. K.: Assessing the Iterative Finite Difference Mass Balance and 4D-Var Methods to Derive Ammonia Emissions Over North America Using Synthetic Observations, J. Geophys. Res.-Atmos., 124, 4222–4236, https://doi.org/10.1029/2018jd030183, 2019.

Li, M., Zhang, Z., Yao, Q., Wang, T., Xie, M., Li, S., Zhuang, B., and Han, Y.: Nonlinear responses of particulate nitrate to NO_x emission controls in the megalopolises of China, Atmos. Chem. Phys., 21, 15135–15152, https://doi.org/10.5194/acp-21-15135-2021, 2021.

Lin, H., Jacob, D. J., Lundgren, E. W., Sulprizio, M. P., Keller, C. A., Fritz, T. M., Eastham, S. D., Emmons, L. K., Campbell, P. C., Baker, B., Saylor, R. D., and Montuoro, R.: Harmonized Emissions Component (HEMCO) 3.0 as a versatile emissions component for atmospheric models: application in the GEOS-Chem, NASA GEOS, WRF-GC, CESM2, NOAA GEFS-Aerosol, and NOAA UFS models, Geosci. Model Dev., 14, 5487–5506, https://doi.org/10.5194/gmd-14-5487-2021, 2021.

Lin, J.-T. and McElroy, M. B.: Impacts of boundary layer mixing on pollutant vertical profiles in the lower troposphere: Implications to satellite remote sensing, Atmos. Environ., 44, 1726–1739, https://doi.org/10.1016/j.atmosenv.2010.02.009, 2010.

Lin, S.-J. and Rood, R. B.: Multidimensional Flux-Form Semi-Lagrangian Transport Schemes, Mon. Weather Rev., 124, 2046–2070, https://doi.org/10.1175/1520-0493(1996)124<2046:MFFSLT>2.0.CO;2, 1996.

Liu, H., Jacob, D. J., Bey, I., and Yantosca, R. M.: Constraints from ^{210}Pb and ^{7}Be on wet deposition and transport in a global three-dimensional chemical tracer model driven by assimilated meteorological fields, J. Geophys. Res.-Atmos., 106, 12109–12128, https://doi.org/10.1029/2000jd900839, 2001.

Liu, J. and Capps, S. L.: Nonlinear Contributions of NOx and Volatile Chemical Products to Air Pollution and the Associated Acute Premature Mortality, ACS ES&T Air, 3, 1462–1472, https://doi.org/10.1021/acsestair.5c00415, 2026.

Liu, J., Chen, E., and Capps, S. L.: The first application of a numerically exact, higher-order sensitivity analysis approach for atmospheric modelling: implementation of the hyperdual-step method in the Community Multiscale Air Quality Model (CMAQ) version 5.3.2, Geosci. Model Dev., 17, 567–585, https://doi.org/10.5194/gmd-17-567-2024, 2024.

Lyu, C., Capps, S. L., Hakami, A., Zhao, S., Resler, J., Carmichael, G. R., Sandu, A., Russell, A. G., Chai, T., and Henze, D. K.: Elucidating emissions control strategies for ozone to protect human health and public welfare within the continental United States, Environ. Res. Lett., 14, 124093, https://doi.org/10.1088/1748-9326/ab5e05, 2019.

Lyu, C., Capps, S. L., Kurashima, K., Henze, D. K., Pierce, G., Hakami, A., Zhao, S., Resler, J., Carmichael, G. R.,

Sandu, A., Russell, A. G., Chai, T., and Milford, J.: Evaluating oil and gas contributions to ambient nonmethane hydrocarbon mixing ratios and ozone-related metrics in the Colorado Front Range, Atmos. Environ., 246, 118113, https://doi.org/10.1016/j.atmosenv.2020.118113, 2021.

Maasakkers, J. D., Jacob, D. J., Sulprizio, M. P., Scarpelli, T. R., Nesser, H., Sheng, J.-X., Zhang, Y., Hersher, M., Bloom, A. A., Bowman, K. W., Worden, J. R., Janssens-Maenhout, G., and Parker, R. J.: Global distribution of methane emissions, emission trends, and OH concentrations and trends inferred from an inversion of GOSAT satellite data for 2010–2015, Atmos. Chem. Phys., 19, 7859–7881, https://doi.org/10.5194/acp-19-7859-2019, 2019.

Mao, Y. H., Li, Q. B., Henze, D. K., Jiang, Z., Jones, D. B. A., Kopacz, M., He, C., Qi, L., Gao, M., Hao, W.-M., and Liou, K.-N.: Estimates of black carbon emissions in the western United States using the GEOS-Chem adjoint model, Atmos. Chem. Phys., 15, 7685–7702, https://doi.org/10.5194/acp-15-7685-2015, 2015.

Martin, R. V., Eastham, S. D., Bindle, L., Lundgren, E. W., Clune, T. L., Keller, C. A., Downs, W., Zhang, D., Lucchesi, R. A., Sulprizio, M. P., Yantosca, R. M., Li, Y., Estrada, L., Putman, W. M., Auer, B. M., Trayanov, A. L., Pawson, S., and Jacob, D. J.: Improved advection, resolution, performance, and community access in the new generation (version 13) of the high-performance GEOS-Chem global atmospheric chemistry model (GCHP), Geosci. Model Dev., 15, 8731–8748, https://doi.org/10.5194/gmd-15-8731-2022, 2022.

Martins, J. R. R. A., Sturdza, P., and Alonso, J. J.: The complex-step derivative approximation, ACM T. Math. Software, 29, 245–262, https://doi.org/10.1145/838250.838251, 2003.

Miller, S. J., Makar, P. A., and Lee, C. J.: HETerogeneous vectorized or Parallel (HETPv1.0): an updated inorganic heterogeneous chemistry solver for the metastable-state NH_4^+–Na^+–Ca^{2+}–K^+–Mg^{2+}–SO_4^{2-}–NO_3^-–Cl^-–H_2O system based on ISORROPIA II, Geosci. Model Dev., 17, 2197–2219, https://doi.org/10.5194/gmd-17-2197-2024, 2024.

Moon, J., Choi, Y., Jeon, W., Kim, H. C., Pouyaei, A., Jung, J., Pan, S., Kim, S., Kim, C. H., Bak, J., Yoo, J. W., Park, J., and Kim, D.: Hybrid IFDMB/4D-Var inverse modeling to constrain the spatiotemporal distribution of CO and NO2 emissions using the CMAQ adjoint model, Atmos. Environ., 327, 10, https://doi.org/10.1016/j.atmosenv.2024.120490, 2024.

Napelenok, S. L., Cohan, D. S., Hu, Y., and Russell, A. G.: Decoupled direct 3D sensitivity analysis for particulate matter (DDM-3D/PM), Atmos. Environ., 40, 6112–6121, https://doi.org/10.1016/j.atmosenv.2006.05.039, 2006.

O'Rourke, P. R., Smith, S. J., Mott, A., Ahsan, H., McDuffie, E. E., Crippa, M., Klimont, Z., McDonald, B., Wang, S., Nicholson, M. B., Feng, L., and Hoesly, R. M.: CEDS v_2021_04_21 Release Emission Data (v_2021_02_05), Zenodo [data set], https://doi.org/10.5281/zenodo.4741285, 2021.

Pai, S. J., Heald, C. L., and Murphy, J. G.: Exploring the Global Importance of Atmospheric Ammonia Oxidation, ACS Earth Space Chem., 5, 1674–1685, https://doi.org/10.1021/acsearthspacechem.1c00021, 2021.

Park, R. J., Jacob, D. J., Field, B. D., Yantosca, R. M., and Chin, M.: Natural and transboundary pollution influences on sulfate-nitrate-ammonium aerosols in the United States: Implications for policy, J. Geophys. Res.-Atmos., 109, https://doi.org/10.1029/2003JD004473, 2004.

Philip, S., Martin, R. V., and Keller, C. A.: Sensitivity of chemistry-transport model simulations to the duration of chemical and transport operators: a case study with GEOS-Chem v10-01, Geosci. Model Dev., 9, 1683–1695, https://doi.org/10.5194/gmd-9-1683-2016, 2016.

Press, W. H., Teukolsky, S. A., Vetterling, W. T., and Flannery, B. P.: Numerical Recipes 3rd Edition: The Art of Scientific Computing, Cambridge University Press, ISBN 9780521880688, 2007.

Pusede, S. E., Duffey, K. C., Shusterman, A. A., Saleh, A., Laughner, J. L., Wooldridge, P. J., Zhang, Q., Parworth, C. L., Kim, H., Capps, S. L., Valin, L. C., Cappa, C. D., Fried, A., Walega, J., Nowak, J. B., Weinheimer, A. J., Hoff, R. M., Berkoff, T. A., Beyersdorf, A. J., Olson, J., Crawford, J. H., and Cohen, R. C.: On the effectiveness of nitrogen oxide reductions as a control over ammonium nitrate aerosol, Atmos. Chem. Phys., 16, 2575–2596, https://doi.org/10.5194/acp-16-2575-2016, 2016.

Pye, H. O. T., Liao, H., Wu, S., Mickley, L. J., Jacob, D. J., Henze, D. K., and Seinfeld, J. H.: Effect of changes in climate and emissions on future sulfate-nitrate-ammonium aerosol levels in the United States, J. Geophys. Res.-Atmos., 114, https://doi.org/10.1029/2008jd010701, 2009.

Qu, Z., Henze, D. K., Capps, S. L., Wang, Y., Xu, X. G., Wang, J., and Keller, M.: Monthly top-down NOx emissions for China (2005–2012): A hybrid inversion method and trend analysis, J. Geophys. Res.-Atmos., 122, 4600–4625, https://doi.org/10.1002/2016jd025852, 2017.

Qu, Z., Henze, D. K., Worden, H. M., Jiang, Z., Gaubert, B., Theys, N., and Wang, W.: Sector-Based Top-Down Estimates of NO_x, SO_2, and CO Emissions in East Asia, Geophys. Res. Lett., 49, https://doi.org/10.1029/2021gl096009, 2022.

Romero-Alvarez, J., Lupaşcu, A., Lowe, D., Badia, A., Archer-Nicholls, S., Dorling, S., Reeves, C. E., and Butler, T.: Sources of surface O_3 in the UK: tagging O_3 within WRF-Chem, Atmos. Chem. Phys., 22, 13797–13815, https://doi.org/10.5194/acp-22-13797-2022, 2022.

Sandu, A. and Sander, R.: Technical note: Simulating chemical systems in Fortran90 and Matlab with the Kinetic PreProcessor KPP-2.1, Atmos. Chem. Phys., 6, 187–195, https://doi.org/10.5194/acp-6-187-2006, 2006.

Seinfeld, J. H. and Pandis, S. N.: Atmospheric chemistry and physics: from air pollution to climate change, 3rd edn., Hoboken, New Jersey, John Wiley & Sons, ISBN 978-1-118-94740-1, 2016.

Sitwell, M., Shephard, M. W., Rochon, Y., Cady-Pereira, K., and Dammers, E.: An ensemble-variational inversion system for the estimation of ammonia emissions using CrIS satellite ammonia retrievals, Atmos. Chem. Phys., 22, 6595–6624, https://doi.org/10.5194/acp-22-6595-2022, 2022.

Squire, W. and Trapp, G.: Using Complex Variables to Estimate Derivatives of Real Functions, SIAM Rev., 40, 110–112, https://doi.org/10.1137/s003614459631241x, 1998.

Sun, H. W., Eastham, S., and Keith, D.: Developing a Plume-in-Grid Model for Plume Evolution in the Stratosphere, J. Adv. Model. Earth Sy., 14, 17, https://doi.org/10.1029/2021ms002816, 2022.

The International GEOS-Chem User Community: geoschem/GC-Classic: GEOS-Chem Classic 14.0.0, Zenodo [code], https://doi.org/10.5281/zenodo.7254984, 2022.

Tian, D., Cohan, D. S., Napelenok, S., Bergin, M., Hu, Y. T., Chang, M., and Russell, A. G.: Uncertainty Analysis of Ozone Formation and Response to Emission Controls Using Higher-Order Sensitivities, J. Air Waste Manage., 60, 797–804, https://doi.org/10.3155/1047-3289.60.7.797, 2010.

Tsimpidi, A. P., Karydis, V. A., and Pandis, S. N.: Response of inorganic fine particulate matter to emission changes of sulfur dioxide and ammonia: The eastern United States as a case study, J. Air Waste Manage., 57, 1489–1498, https://doi.org/10.3155/1047-3289.57.12.1489, 2007.

Turner, M. C., Jerrett, M., Pope III, C. A., Krewski, D., Gapstur, S. M., Diver, W. R., Beckerman, B. S., Marshall, J. D., Su, J., Crouse, D. L., and Burnett, R. T.: Long-Term Ozone Exposure and Mortality in a Large Prospective Study, Am. J. Resp. Crit. Care, 193, 1134–1142, https://doi.org/10.1164/rccm.201508-1633OC, 2016.

Turner, M. D., Henze, D. K., Capps, S. L., Hakami, A., Zhao, S., Resler, J., Carmichael, G. R., Stanier, C. O., Baek, J., Sandu, A., Russell, A. G., Nenes, A., Pinder, R. W., Napelenok, S. L., Bash, J. O., Percell, P. B., and Chai, T.: Premature deaths attributed to source-specific BC emissions in six urban US regions, Environ. Res. Lett., 10, https://doi.org/10.1088/1748-9326/10/11/114014, 2015.

Utke, J., Naumann, U., Fagan, M., Tallent, N., Strout, M., Heimbach, P., Hill, C., and Wunsch, C.: OpenAD/F: A modular open-source tool for automatic differentiation of Fortran codes, ACM T. Math. Software, 34, 36, https://doi.org/10.1145/1377596.1377598, 2008.

van der Graaf, S., Dammers, E., Segers, A., Kranenburg, R., Schaap, M., Shephard, M. W., and Erisman, J. W.: Data assimilation of CrIS NH_3 satellite observations for improving spatiotemporal NH_3 distributions in LOTOS-EUROS, Atmos. Chem. Phys., 22, 951–972, https://doi.org/10.5194/acp-22-951-2022, 2022.

Varon, D. J., Jacob, D. J., Sulprizio, M., Estrada, L. A., Downs, W. B., Shen, L., Hancock, S. E., Nesser, H., Qu, Z., Penn, E., Chen, Z., Lu, X., Lorente, A., Tewari, A., and Randles, C. A.: Integrated Methane Inversion (IMI 1.0): a user-friendly, cloud-based facility for inferring high-resolution methane emissions from TROPOMI satellite observations, Geosci. Model Dev., 15, 5787–5805, https://doi.org/10.5194/gmd-15-5787-2022, 2022.

Vinken, G. C. M., Boersma, K. F., Jacob, D. J., and Meijer, E. W.: Accounting for non-linear chemistry of ship plumes in the GEOS-Chem global chemistry transport model, Atmos. Chem. Phys., 11, 11707–11722, https://doi.org/10.5194/acp-11-11707-2011, 2011.

Vukicevic, T. and Errico, R. M.: LINEARIZATION AND ADJOINT OF PARAMETERIZED MOIST DIABATIC PROCESSES, Tellus A, 45, 493–510, https://doi.org/10.1034/j.1600-0870.1993.0012.x, 1993.

Wang, X. M., Carmichael, G., Chen, D. L., Tang, Y. H., and Wang, T. J.: Impacts of different emission sources on air quality during March 2001 in the Pearl River Delta (PRD) region, Atmos. Environ., 39, 5227–5241, https://doi.org/10.1016/j.atmosenv.2005.04.035, 2005.

Wang, Y., Zhang, Y., Hao, J., and Luo, M.: Seasonal and spatial variability of surface ozone over China: contributions from background and domestic pollution, Atmos. Chem. Phys., 11, 3511–3525, https://doi.org/10.5194/acp-11-3511-2011, 2011.

Wang, Y. H., Jacob, D. J., and Logan, J. A.: Global simulation of tropospheric O-3-NOx-hydrocarbon chemistry 1. Model formulation, J. Geophys. Res.-Atmos., 103, 10713–10725, https://doi.org/10.1029/98JD00158, 1998.

Wesely, M. L.: Parameterization of surface resistances to gaseous dry deposition in regional-scale numerical models, Atmos. Environ., 23, 1293–1304, https://doi.org/10.1016/0004-6981(89)90153-4, 1989.

Whaley, C. H., Strong, K., Jones, D. B. A., Walker, T. W., Jiang, Z., Henze, D. K., Cooke, M. A., McLinden, C. A., Mittermeier, R. L., Pommier, M., and Fogal, P. F.: Toronto area ozone: Long-term measurements and modeled sources of poor air quality events, J. Geophys. Res.-Atmos., 120, 11368–11390, https://doi.org/10.1002/2014jd022984, 2015.

Yan, Y., Cabrera-Perez, D., Lin, J., Pozzer, A., Hu, L., Millet, D. B., Porter, W. C., and Lelieveld, J.: Global tropospheric effects of aromatic chemistry with the SAPRC-11 mechanism implemented in GEOS-Chem version 9-02, Geosci. Model Dev., 12, 111–130, https://doi.org/10.5194/gmd-12-111-2019, 2019.

Yang, J. Y. and Zhao, Y.: Performance and application of air quality models on ozone simulation in China – A review, Atmos. Environ., 293, 20, https://doi.org/10.1016/j.atmosenv.2022.119446, 2023.

Yang, Y.-J., Wilkinson, J. G., and Russell, A. G.: Fast, direct sensitivity analysis of multidimensional photochemical models, Environ. Sci. Technol., 31, 2859–2868, https://doi.org/10.1021/es970117w, 1997.

Ying, Q. and Kleeman, M. J.: Source contributions to the regional distribution of secondary particulate matter in California, Atmos. Environ., 40, 736–752, https://doi.org/10.1016/j.atmosenv.2005.10.007, 2006.

Zhang, L., Shao, J. Y., Lu, X., Zhao, Y. H., Hu, Y. Y., Henze, D. K., Liao, H., Gong, S. L., and Zhang, Q.: Sources and Processes Affecting Fine Particulate Matter Pollution over North China: An Adjoint Analysis of the Beijing APEC Period, Environ. Sci. Technol., 50, 8731–8740, https://doi.org/10.1021/acs.est.6b03010, 2016.

Zhang, W., Capps, S. L., Hu, Y., Nenes, A., Napelenok, S. L., and Russell, A. G.: Development of the high-order decoupled direct method in three dimensions for particulate matter: enabling advanced sensitivity analysis in air quality models, Geosci. Model Dev., 5, 355–368, https://doi.org/10.5194/gmd-5-355-2012, 2012.

Zhang, Y., Tang, L., Sun, Y., Favez, O., Canonaco, F., Albinet, A., Couvidat, F., Liu, D., Jayne, J. T., Wang, Z., Croteau, P. L., Canagaratna, M. R., Zhou, H.-C., Prévôt, A. S. H., and Worsnop, D. R.: Limited formation of isoprene epoxydiols-derived secondary organic aerosol under NOx-rich environments in Eastern China, Geophys. Res. Lett., 44, 2035–2043, https://doi.org/10.1002/2016GL072368, 2017.

Zhang, Y. Z., Gautam, R., Pandey, S., Omara, M., Maasakkers, J. D., Sadavarte, P., Lyon, D., Nesser, H., Sulprizio, M. P., Varon, D. J., Zhang, R. X., Houweling, S., Zavala-Araiza, D., Alvarez, R. A., Lorente, A., Hamburg, S. P., Aben, I., and Jacob, D. J.: Quantifying methane emissions from the largest oil-producing basin in the United States from space, Sci. Adv., 6, 9, https://doi.org/10.1126/sciadv.aaz5120, 2020.

Zhao, S., Russell, M. G., Hakami, A., Capps, S. L., Turner, M. D., Henze, D. K., Percell, P. B., Resler, J., Shen, H., Russell, A. G.,

Nenes, A., Pappin, A. J., Napelenok, S. L., Bash, J. O., Fahey, K. M., Carmichael, G. R., Stanier, C. O., and Chai, T.: A multiphase CMAQ version 5.0 adjoint, Geosci. Model Dev., 13, 2925–2944, https://doi.org/10.5194/gmd-13-2925-2020, 2020.

Zhao, Y. S., Li, Y. T., Kumar, A., Ying, Q., Vandenberghe, F., and Kleeman, M. J.: Separately resolving NOx and VOC contributions to ozone formation, Atmos. Environ., 285, 15, https://doi.org/10.1016/j.atmosenv.2022.119224, 2022.

Zheng, T., French, N. H. F., and Baxter, M.: Development of the WRF-CO2 4D-Var assimilation system v1.0, Geosci. Model Dev., 11, 1725–1752, https://doi.org/10.5194/gmd-11-1725-2018, 2018.

Zhu, L., Henze, D., Bash, J., Jeong, G.-R., Cady-Pereira, K., Shephard, M., Luo, M., Paulot, F., and Capps, S.: Global evaluation of ammonia bidirectional exchange and livestock diurnal variation schemes, Atmos. Chem. Phys., 15, 12823–12843, https://doi.org/10.5194/acp-15-12823-2015, 2015.